An integrated view of the methane system in the pockmarks at Vestnesa Ridge, 79°N

Giuliana Panieri, Stefan Bünz, Daniel J Fornari, Javier Escartin, Pavel Serov, Pär Jansson, Marta Torres, Joel Johnson, Weili Hong, Simone Sauer, et al.

An integrated view of the methane system in the pockmarks at Vestnesa Ridge, 79°N

Giuliana Panieri[1]*, Stefan Bünz[1], Daniel J. Fornari[2], Javier Escartin[3], Pavel Serov[1], Pär Jansson[1], Marta E. Torres[4], Joel E. Johnson[5], WeiLi Hong[1,6], Simone Sauer[6,1], Rafael Garcia[7], Nuno Gracias[7]

[1] CAGE—Centre for Arctic Gas Hydrate, Environment and Climate, Department of Geosciences, UiT The Arctic University of Norway, 9037 Tromsø, Norway

[2] Woods Hole Oceanographic Institution, Geology & Geophysics Dept., Woods Hole, MA 02543 USA

[3]Groupe de Geosciences Marines, IPGP, CNRS UMR7154, Paris, France

[4]College of Earth, Ocean and Atmospheric Sciences, Oregon State University, Corvallis, OR USA

[5]Department of Earth Sciences, University of New Hampshire, Durham, NH, USA

[6]Gelogical Survey of Norway, Trondheim, Norway

[7]Computer Vision and Robotics Institute, University of Girona, Girona, Spain

*corresponding author

Abstract

The Vestnesa Ridge is a NW-SE trending, ~100 km-long, 1-2 km-thick contourite sediment section located in the Arctic Ocean, west of Svalbard, at 79°N. Pockmarks align along the ridge summit at water depths of ~1200 m; they are ~700 m in diameter and ~10 m deep relative to the surrounding seafloor. Observations of methane seepage in this area have been reported since 2008. Here we summarize and integrate the available information to date and report on the first detailed seafloor imaging and camera-guided multicore sampling at two of the most active pockmarks along Vestnesa Ridge, named Lomvi and Lunde. We correlate seafloor images with

seismically defined subseafloor structures, providing a geological and ecological context to better understand pockmark formation and water column observations. Subbottom and seismic surveys, water column imaging, geochemical data and seafloor observations indicate ongoing fluid flow at these pockmarks. Visual inspection and sampling using a high-resolution deep-sea camera and multicorer system show exposed gas hydrate and authigenic carbonate in association with biota within two of these pockmarks. Distributed methane venting at both Lomvi and Lunde supports extensive chemosynthetic communities that include filamentous sulphide-oxidizing bacteria and Siboglinid tubeworms, all of which utilize chemical energy provided by the seeping fluids. Focused venting forms shallow gas hydrate, and sustains localized gas discharge from 50-m wide pits within the pockmarks. Cycles of carbonate precipitation and/or exhumation of carbonate deposits are indicated by scattered blocks of various size, pavements, and massive carbonate blocks up to 3 m. Consistent with other observations along continental margin settings, we show that the extensive authigenic carbonate deposits in the Vestnesa pockmarks represent an important and prolonged methane sink that prevents much of the upwardly flowing methane from reaching the overlying ocean.

Keywords: Fluid expulsions, methane, pockmarks, gas flares, seeps, gas hydrate, photomosaicing, carbonate concretions, chemosynthetic organisms, Vestnesa, Arctic Ocean

1. Introduction

Pockmarks are a common morphological expression of gas and fluid seepage within marine sediment (Judd and Hovland, 2007). These depressions occur primarily along continental margins worldwide, often overlying hydrocarbon reservoirs. Pockmarks are generated by erosional processes associated with lift and suspension of sediment by upward-migrating aqueous and gas fluids (e.g., Hovland, 1981; Hovland and Judd, 1988), and as such are often

associated with focused fluid flow pathways in the subseabed (Hovland et al., 1985, Løseth et al., 2009, Plaza-Faverola et al., 2015). Pockmarks have also been explained as resulting from sediment compaction and overpressure dissipation via fluid flow (O´Regan et al., 2015). In seismic data, gas migration pathways are imaged as sub-vertical zones that exhibit acoustic masking and disruption in the continuity of seismic reflectors over vertical extents of tens to hundreds of meters, usually referred to as acoustic chimneys.

In the eastern Fram Strait west of Svalbard (~79°N), fields of pockmarks occur along the crest of the Vestnesa Ridge (Fig. 1). Discovered in 1994 (Vogt et al., 1994), these pockmarks consist of semi-circular seafloor depressions up to 700 m in diameter and as deep as 10 m. They exhibit active venting of methane-rich fluids from confined deep-water gas hydrate and free gas reservoirs (Bünz et al., 2012). At least six of the pockmarks along the eastern sector of Vestnesa Ridge actively release methane into the water column forming gas bubble streams (Fig. 1b) that reach heights of up to 1 km above the seafloor (Smith et al., 2014).

The two dominant methane producing processes in marine sediments are: (i) methane generated by methanogenic archaea (Rice and Claypool, 1981), known as ‘biogenic’ or ‘microbial’ methane; and (ii) methane generated during the thermally-driven break-down of larger organic molecules at temperatures above 150°C (e.g. Clayton, 1991), termed ‘thermogenic’ methane. The molecular (ratio of methane to other hydrocarbons) and isotopic composition (^{13}C-CH_4) of methane changes depending on its origin. Biogenic gas is predominantly methane, whereas thermogenic gas contains a larger fraction of higher-order hydrocarbons. Isotopic values of thermogenic methane range between− 50‰ and − 20‰, whereas values ranging from − 110‰ and − 50‰ characterize for microbial methane (Whiticar et al., 1999).

Methane migrating through the sediments is anaerobically oxidized by a microbial consortium of sulfate reducing bacteria and methanotrophic archaea (Boetius et al., 2000) at the methane-sulfate transition (SMT), which marks the downcore limit of sulfate diffusing into the sediment

from the overlying seawater. The anaerobic oxidation of methane (AOM) generates sulfide and excess alkalinity. Enhanced alkalinity drives the precipitation of methane-derived authigenic carbonates (MDAC), which form crusts and concretions within anoxic sediments or at the seafloor (Aloisi et al., 2000, 2002; Bayon et al., 2013; Crémière et al., 2013; Luff et al., 2004; Peckmann et al., 2001). The release of reducing fluids at the seafloor sustains monospecific or low-diversity chemosynthetic communities (Taviani, 2001). Several modern seep communities are dominated by Siboglinid tubeworms (vestimentiferans and frenulates; see Rouse, 2001 for systematics of this group), as well as vesicomyid and bathymodioline bivalves and also contain lucinid, thyasirid, and solemyid bivalves (Sibuet and Olu, 1998).

Here, we provide the first evidence for the presence of extensive authigenic carbonate formation, and for chemosynthetic communities within pockmarks along the Vestnesa Ridge, a deep-water carbon sink that prevents much of the methane from reaching bottom water. We provide a holistic view of the methane seep system at Vestnesa by relating seafloor carbonate structures to seismically imaged subseafloor features, and integrating these data with seafloor imagery, precisely controlled sampling, core logs, gas flares imaged acoustically and hydrocarbon analyses. We further interpret our results in the context of significant findings in this region during the past decade (Table 1), and present an integrated scenario for methane budgets in this active pockmark area (Table 3). Seismic data indicate that there are significant amounts of methane and gas hydrate within the acoustic chimney structure below Lomvi and Lunde (Bünz et al., 2012). Geochemical and geophysical evidence shows that the pockmarks are characterized by both focused and diffuse fluid flow. A comparison with other carbonate records from gravity cores in this region show that methane release and consumption processes currently observed at the Vestnesa pockmarks have been ongoing since at least the last deglaciation, from 20,000 to 15,000 yrs BP (Ambrose et al., 2015).

100 Data presented here are placed in a context of current understanding of methane systematics in
101 the Vestnesa pockmark system and are compared with other pockmark regions, providing a
102 synthesis of the state of our knowledge, which can serve as a platform for ongoing and future
103 efforts aimed at evaluating the impact of increasing methane discharge on the Arctic seafloor
104 environment and elsewhere.
105
106 **2. Geological setting**
107 Vestnesa Ridge is a 100 km long submarine sediment drift located at the eastern spreading
108 segments of the Molloy Ridge off the west Svalbard margin (Fig. 1a). It is situated on relatively
109 young (<20 Ma) and hot oceanic crust, with an estimated heat flux of >115 mW/m^2 (Eiken and
110 Hinz, 1993; Engen et al., 2008; Hustoft et al., 2009). The ridge is elongated and bends from a
111 SE-NW to E-W direction, with a summit pierced by pockmarks at 1200-1300 m depth (Fig. 1b)
112 (Bünz et al., 2012).
113 The sediment thickness along the Vestnesa Ridge increases from 1 km in the west to >2 km at its
114 eastern end (Vogt al., 1994). The shallow stratigraphy is comprised of contourite, turbidite and
115 hemipelagic sediments that have been partly reworked by ocean bottom currents (Howe et al.,
116 2008). The seismically defined stratigraphy is divided into three main sequences: YP1, YP2, and
117 YP3, from oldest to youngest (Figure 10 in; Eiken and Hinz, 1993). Section YP1 consist of syn-
118 and post-rift deposits above the oceanic crust (Hustoft et al., 2009), whereas YP2 is characterized
119 by contourites. The basal age of the YP-2 contouritic sequence beneath Vestnesa Ridge could be
120 at least 11 Ma (Mattingsdal et al., 2014), while in the offset drift south of the MTF it may be
121 closer to 2 Ma (Johnson et al., 2015). The YP2/YP3 boundary represents an unconformity
122 throughout Fram Strait, marking the onset of the Plio-Pleistocene glaciations (Eiken and Hinz,
123 1993; Hustoft et al., 2009; Knies et al., 2009). The youngest sediments covering the crest of the

ridge consist primarily of silty turbidites and muddy-silty contourites from late Weichselian to Holocene age (Howe et al., 2008).

A bottom-simulating reflection (BSR) is observed in seismic data south of the MTF and over large parts of the western Svalbard Margin (Hustoft et al., 2009; Johnson et al., 2015, Dumke et al., 2016). The BSR marks the base of the gas-hydrate stability zone (GHSZ) (Stoll et al., 1971), and originates from a strong impedance contrast of partially hydrate-saturated sediments above and gas-charged sediments below this boundary. Gas bubble streams emerging from the seafloor are commonly imaged as 'acoustic flares' on echograms (Greinert et al., 2006; Naudts et al., 2006), and are taken as indicators of active gas seepage (Greinert, 2008; Veloso et al., 2015; Römer et al., 2014). In the eastern sector of Vestnesa the pockmarks are active as indicated by prevailing acoustic flares (Hustoft et al., 2009; Bünz et al., 2012; Smith et al., 2014), whereas the western sector appears to be inactive at the present time. Acoustic chimneys imaged seismically beneath most of the pockmarks along the ridge can be attributed to advection of free-gas from beneath the BSR towards the shallow subsurface. Chimney distribution appears related to faults and fractures that reflect the influence of nearby tectonic stress fields, including rifting at the Molloy and Knipovich Ridges, as well as to shear motion along the Spitsbergen Transform Fault (Plaza-Faverola et al., 2015).

3. Methods

Here we present new data from cruises conducted on R/V *Helmer Hanssen* to the Vestnesa Ridge in 2015, and complement our findings with multidisciplinary data collected in this region by the CAGE group and collaborators since 2010. The surveys and data acquired are summarized in Table 1, which includes additional data and published results used in this paper.

3.1 Geophysical surveys

149 Geophysical data acquired during several R/V *Helmer Hanssen* cruises between 2010 and 2015
150 include multibeam bathymetry, single-beam echo sounding, and 3D seismic data (Table 1).
151 These surveys provide the bathymetric and sub-seabed context to interpret the nature and history
152 of the Vestnesa Ridge pockmarks, and water column acoustic data to understand the distribution
153 and time variability of gas release from the seafloor. The majority of these data have been
154 published (Table 1), and in this study we correlate the previously mapped subsurface features
155 with our new seafloor and water column observations. We thus include here only a brief
156 overview of the geophysical methods used.
157 Swath bathymetry data were acquired using a hull-mounted Kongsberg Simrad EM-300 system
158 (Fig. 1) that was operated simultaneously with the 3D seismic survey (Smith et al., 2014; Plaza-
159 Faverola et al., 2015). Due to the close spacing of the 3D seismic acquisition lines (~50 m) and
160 the wide angular coverage of the multibeam system, the bathymetric data coverage in the area of
161 the 3D seismic survey is significantly denser and of higher resolution, which allowed us to
162 generate grids with only a 10 m spacing (Fig. 2a).
163
164 *3.1.1 Single-beam echo sounding and methane flow rate calculation*
165 Single-beam echo sounding data were acquired during several cruises (Table 1) using a Simrad
166 EK60 system operating at frequencies of 18 and 38 kHz. While this system is mainly used for
167 depth sounding, it also detects gas flares in the water column. The © Fledermaus Midwater
168 module was used to process and extract acoustic flares from the echosounder data. Individual
169 flares are imaged on multiple, parallel acquisition lines of the 3D seismic survey (Fig. 1b).
170 To obtain a first broad estimate of free gas methane fluxes emitted from Lomvi and Lunde, we
171 used backscatter target strength (TS) from the 38 kHz channel of the Simrad EK60 echosounder
172 in the water layer between 5 and 10 m above the seafloor to avoid seafloor scatter induced by the
173 motion of the ship.. We manually removed instrument interference and converted flare-

representative target strength values (dB) to cross sections and subsequently to *in-situ* gas flow rates (ml min^{-1}) (e.g., Medwin and Clay, 1997; Ona, 1999).

In our calculations (detailed in the Supplementary data: Methods and Tables 1SD-3SD) we assumed spherical bubbles without hydrate coating. Some of the parameters used in the flux calculations are not well constrained. For example, as we do not have direct observations of bubble size we use minimum and maximum bubble sizes of 3 and 8 mm, with rising speeds of 15 to 30 cm s^{-1} (see Supplementary data for details on parameter assumptions and associated references). We also restrict our analysis to data acquired in 2012 over the Lomvi and Lunde as gas flare activity was high relative to 2010 and low relative to 2013 and 2015. A temporal study of flux variations is out of the scope of this study; an in depth analysis of these data will be presented in a future paper.

3.1.2 High-resolution P-cable 3D seismic data

High-resolution 3D seismic data presented in this paper (Fig. 2) were acquired in 2013 using the P-Cable seismic system (Planke et al., 2009). Details on the acquisition and processing parameters can be found in Plaza-Faverola et al. (2015). The resulting 3D seismic data has a spatial resolution of 6.25 m.

3D seismic interpretation was performed using Schlumberger's Petrel package and included horizon interpretation and attribute mapping. A Root Mean Square (RMS) amplitude volume with a vertical window of 7 ms was derived from seismic data in order to identify and spatially map amplitude anomalies that are mostly related to fluid related features. For visualization, we also applied the spectral method of Partyka et al. (1999) to decompose the data into three spectral components, at frequencies of 100 (red), 150 (green) and 220 Hz (blue) (Fig. 2). Volume colour blending of these three components was used to image the upper few meters of the pockmark structures on the Vestnesa Ridge in order to identify impedance contrasts associated with

carbonate accretions, gas hydrates, gas, shell beds, fluidized feeder pathways and the thickness of infilling sediments.

3.2 Seafloor imagery

Visual seafloor observations were made during the 2015 CAGE15-2 R/V *Helmer Hanssen* expedition, using a modified *TowCam* deep-sea imaging system (Fornari, 2003). The *TowCam* system was developed at the Woods Hole Oceanographic Institution's (WHOI) Multidisciplinary Instrumentation in Support of Oceanography (MISO) Facility. It is equipped with a 16 megapixel deep-sea color digital camera, a real-time Conductivity, Temperature, Depth (CTD) instrument, and an altimeter (http://www.whoi.edu/main/instruments/miso), with real time transmission of images and data. For this study, the *TowCam* was integrated with the UiT-NPI (UiT -The Arctic University of Norway and NPI - Norwegian Polar Institute) multi-corer. The combined *TowCam-Multicorer system* (TC-MC) was used to visually survey and sample sediments from the Lunde and Lomvi pockmarks (Fig. 1c). High-resolution images were collected in order to select sampling targets, to visually describe seafloor textures and indicators of fluid activity, and to identify areas with chemosynthetic fauna and authigenic carbonates (Figs. 3, 4, and 5).

To facilitate geological and biological observations, TC-MC imagery was first processed to correct for variations in illumination. The corrected images where then used to identify matching points where overlap between images existed, and to re-navigate the camera positions. Georeferenced photomosaics (Fig. 3, and Fig. 1SD in Supplementary data) were generated from the re-navigated images, projected and blended to remove image seams and corrected for differences in color. Details regarding image processing and mosaic construction are available elsewhere (Prados et al., 2014). In our study area, we generated three photomosaics, with a pixel resolution of 5 mm (Fig. 1SD in Supplementary data). The georeferenced mosaics are

subsequently used for geological interpretation (Fig. 3) integrated with the other datasets presented here.

3.3. Core sampling

Sediment samples from Lunde and Lomvi pockmarks used for gas measurements were collected during the CAGE15-2 cruise using gravity cores (15-2-890GC, Table 2) and the TC-MC multicorer system that allowed for the collection of six 60 cm-long, real-time visually-guided cores (15-2-886MC and 15-2-893MC, Table 2). Selection of sites where the TC-MC instrument was deployed along the six survey lines shown in Fig. 1c was determined using multibeam bathymetry and hydroacoustic data. We complement these data with additional gravity cores collected at depths of ~1200 m during the CAGE13 cruise: core HH13-203GC show evidence of gas hydrate and core HH13-204GC penetrated a discrete chemosynthetic bivalve shell horizon and contains methane-derived carbonate concretions at ~1.5 mbsf (Table 2).

3.4 Gas analyses

Gas hydrate retrieved in core 15-2-893MC was allowed to decompose and the gas released was collected into a vacuum chamber. Interstitial gas from sediments in cores HH13-203GC, HH13-204GC, CAGE15-2-886MC and 15-2-890GC was sampled using the conventional headspace technique described by Hoehler et al. (2000). Gas analyses were performed with a ThermoScientific Trace 1310 gas chromatograph equipped with a ThermoScientific TG-BOND alumina (30m x 0,53mm x 10µm column) and a flame-ionization detector (GC-FID).

Carbon and hydrogen isotope analyses of methane samples from core HH13-203GC were analyzed at Hydroisotop GmbH, Germany, with a GC-MS-IRMS system (Thermo Fischer Scientific GmbH). The analytical precision of $\delta^{13}C$ and δD was ±1.5‰ (1σ) and ±10‰ (1σ), respectively. Carbon and hydrogen isotope analyses of methane samples from the CAGE15-2

249 cruise were conducted at ISOLAB b.v. in the Netherlands. Carbon isotopes of methane were
250 analyzed with an Agilent 6890N GC (Agilent Technologies, Santa Clara, US) interfaced to a
251 Finigan Delta S IRMS using a Finigan GC-C II interface. The GC was equipped with a 12m,
252 0.32mm mol sieve column (Agilent) and an injection valve, and the data reported in per mil (‰)
253 vPDB. For the hydrogen isotopes of methane, the δD measurements were done using an Agilent
254 7890A GC interfaced to a MAT 253 IRMS via the GC-Isolink interface from Thermo. The GC
255 was equipped with a 25m, 0.32mm mol sieve column and an injection valve, and the data are
256 reported in per mil (‰) vSMOW. Instruments were calibrated regularly against a calibration
257 standard and results and the precision of $\delta^{13}C$ and δD measurements was ±1.5‰ (1σ) and ±10‰
258 (1σ), respectively.
259
260 **4. Results**
261 *4.1 Gas flares: location and fluxes*
262 Gas flares have been detected along the crest of the eastern sector of Vestnesa Ridge since 2008,
263 which document methane emission from six pockmarks (Fig. 1b). Cruises in subsequent years
264 confirmed the gas release, showed that it displays short (hourly to daily) to long-term (annual)
265 variation in intensity (Smith et al., 2014), and established the Lomvi and Lunde pockmarks to be
266 the most active. The CAGE 15-2 cruise re-mapped the gas flares emanating from Lomvi and
267 Lunde. We did not observe gas flares reaching the sea surface, but many rise up to 800 m above
268 the seafloor. Flare location guided the deployment of the TC-MC to visually characterize the gas
269 release at the seafloor, which occurs from pits up to 50 m in diameter within the pockmarks.
270 To generate a first order estimate of the methane discharge rates from the Lunde and Lomvi
271 pockmarks, we utilize the EK60 38 kHz records from several cruises (Table 1) and applied the
272 theory and the “FlareHunter” graphical user interface software described in Veloso et al. (2015)
273 that uses intensity of the ecoshounder back scatter (See Supplementary data for details on the

method and inherent uncertainties). The 2012 data show that there are two active flares over the Lomvi pockmark, and three flares over the Lunde pockmark; all have very similar TS values (-52 to -53 dB). By integrating the flare flow rates within each pockmark, and given the uncertainties in our parameters (see Supplementary methods and Table 3SD), we estimate a volumetric total flow rate at Lomvi of 11.6 – 267 ml min^{-1}, while that at Lunde is somewhat lower (8.2 – 187 ml min^{-1}). Assuming that the gas escapes from the smaller pits (radius ~25m), we calculate the free gas flux to range from 13.3 to 395.5 and from 15.7 to 374 mmol m^{-2} d^{-1} in the Lomvi and Lunde pits, respectively. We consider these minimum values as we assumed hydrate-free bubbles. Hydrate coating would modify the acoustic properties of the bubbles (Maksimov, 2005), consequently the methane flux with hydrate coated bubbles could be up to 4 times higher as assumed by Muyashkin and Sauter (2010).

A first order integrated methane output of Lomvi and Lunde was estimated to be of 0.33 – 8.81 tons y^{-1}. This value is considerably lower than the methane flow rate observed at Håkon Mosby Mud Volcano (100 – 400 tons yr^{-1}) (Muyakshin, 2010), and that of Sahling et al. (2014) who estimated a flux of 144 – 1888 tons yr^{-1} from an area of methane seepage west of Prins Karls Forland, Svalbard. Weber et al. (2014) estimated that 1300 – 160,000 tons are emitted yearly from an area of 6,000 km^2 in the Gulf of Mexico, and Shakhova et al. (2014) calculated that 900,000 tons yr^{-1} escapes the seafloor in the East Siberian Arctic Shelf (an area of 18,400 km^2). The variation of almost 2 orders of magnitude in our estimates at Lomvi and Lunde demonstrate that additional observations are required to properly constrain the model parameters (e.g., bubble sizes, hydrate coating, rising speeds) and to obtain better flux estimates. Furthermore, some backscatter data from an event with increased emissions in 2015 suggests fluxes that are larger by two to three orders of magnitude. A more detailed study of methane fluxes associated with individual flares and pockmarks, their distribution, and temporal variability and the spatial and temporal scales at which they may occur, is out of the scope of this paper and is the focus of a

299 future study (Jansson, in prep.).

300

301 *4.2 Visual observations and fine-scale morphology of the Lomvi and Lunde pockmarks*

302 Pockmarks contain complex internal structures with the most notable features being small
303 circular pit-like depressions with diameters of up to 50 m (Fig. 2a-f). Small ridge-like structures
304 with elevations of up to 6 m occur within the pits. They consist of near-vertical stepped walls
305 (Fig. 5) showing rare scattered blocks (<50 cm in size, Fig. 4d), and patches of bacterial mats
306 within the pit floors. The pits generally appear to have an unconsolidated, sedimented bottom.
307 The seismic amplitude information for the region below both Lomvi and Lunde pockmarks
308 shows that the deepest parts of the pits are usually associated with low amplitude anomalies (Fig.
309 2b), as corroborated by the poor response of spectral components at all frequency bands (Fig.
310 2c).

311 We document the presence of three of these pits in Lomvi, located along the perimeter of the
312 main depression (Figs 1c and 2a), whereas in Lunde the three pits mapped are aligned along a N-
313 S axis and at the SW quadrant of the pockmark (Fig. 1c). Amplitude information from the high-
314 resolution 3D seismic data revealed that only the ridge-like structures within the pits have strong
315 impedance contrasts characteristic of hard surfaces (Fig. 2b). Gravity core recovery from these
316 ridges never exceeded 1 m when the recovery was successful (rate recovery 80%), suggesting the
317 presence of hard subsurface deposits within these small ridges. Visual observations from the TC-
318 MC confirmed these hard surfaces to be widespread carbonate, comprising carbonate crusts (~5-
319 10 cm thick, Fig. 4a), scattered blocks (~20-100 cm in size; Fig. 4d), and massive blocks (Fig.
320 4e) that reach 1-5 m in length and up to 3 m in height. Areas where carbonates were observed on
321 the seafloor are well correlated with the whitish to brownish areas in the frequency-decomposed
322 image of the seafloor (Fig. 2c). For example, the largest shift towards lower frequencies occurs

323 at the western rim of Lomvi in the area where the TC-MC imaging has shown massive blocks of
324 carbonate (Fig. 4e).
325
326 *4.3. Subseafloor geometry of pockmark fluid conduits*
327 High-resolution 3D seismic data beneath Lomvi and Lunde show a vertical zone of acoustically
328 transparent and highly disturbed seismic reflections. This vertical zone has been interpreted as an
329 acoustic chimney structure extending from the base of the hydrate-stability zone, denoted by the
330 BSR, up to the seafloor (Bünz et al., 2012). The deepest part of the chimney is characterized by
331 acoustic blanking resulting from scattering and attenuation of seismic energy that increases with
332 depth (Fig. 2e, f). In contrast, the top half of the chimney shows enhanced reflections that appear
333 to cut across lithological boundaries and are slightly inclined towards the seafloor (Plaza-
334 Faverola et al., 2015). By cross-mapping the seismic data with our seafloor observations we
335 show that the enhanced reflections can be traced up to the seafloor where they terminate within
336 the pits identified by TC-MC imaging (Fig. 5). The enhanced reflection results from a strong
337 impedance contrast. Since these acoustically reflective areas can be correlated with the pits at the
338 seafloor where gas seeps into the water column (Fig. 10), our interpretation is that the reflection
339 anomalies result from upward advection of free gas within the chimney, which discharges at pits
340 within the pockmarks and from the occurrence of carbonate layers at or near the seafloor.
341
342 *4.4. Distribution and structure of benthic communities from seafloor observations*
343 Photographic observations were made at altitudes of ~2-6 m above the seafloor with the TC-MC
344 during transects across Lomvi and Lunde and adjacent areas (Fig. 1c). The high-resolution
345 photographs revealed habitat heterogeneity related to carbonate concretions such as pavement
346 and blocks colonized by epibenthic fauna (e.g., sponges, gorgonian corals, anemones, and
347 feather stars), siboglinid tubeworms communities, bacterial mats (Fig. 3), and thin layers of gas

hydrate within the shallow subseafloor (Fig. 7c). These visual observations also reveal both isolated and concentrated angular, ice-rafted clasts at the seafloor within and between Lomvi and Lunde (Fig. 6a), suggesting that sea-ice transport and melting are important contributors of material to the area.

4.4.1 Macrofauna

The macrofaunal density on soft sediments and carbonate outcrops within the pockmarks is high compared to that of nearby seafloor, here considered as background. The sediments host abundant frenulating tubeworms belonging to the family *Siboglinidae* (Fig. 4f) as previously observed (T. Treude, unpubl. data; Smith et al., 2014; Panieri et al., 2015). These organisms have lengths of up to 30 cm, and are exposed 3-4 cm above the seafloor. They are known to necessarily live in a mutualistic association with chemosynthetic bacteria (Hilário et al., 2011). They are important members of deep-sea chemosynthetic communities that include hydrothermal vents, cold seeps and oxygen reduced sediments (Rouse, 2001). During our seafloor surveys with the TC-MC, the frenulating tubeworms were found either sparsely distributed, or grouped in patches of up to 50 cm in diameter. Images of the soft sediment around the carbonate crusts show evidence of recent bioturbation, such as trails of bivalves and other benthic organisms. The carbonate outcrops host a variety of filter feeders and colonies of fauna that typically populate hard substratum environments at cold seeps. These include, among others, epibenthic fauna, large sponges, serpulid tubeworms, anemones, and feather stars. Some of the blocks are densely covered by subspheroidal to spheroidal sponges with an average diameter of ~5 cm (Fig. 4e), most likely belonging to *Cinachyra* (Fig. 4e) (A. Thurber, pers. comm., 2016). We also observed higher trophic-level organisms, such as large predatory or omnivorous species (e.g., fish and sea spiders), which take advantage of the abundant food available around the Vestnesa seeps.

373

374 *4.4.2 Bacterial mats*

375 Patches of bacterial mats have been observed in the central parts of the Lomvi and Lunde
376 pockmarks, particularly within the pits (Fig. 5d). The mats develop on soft sediments and show
377 morphologies that vary from continuous, irregular surfaces ~10 cm to up to ~1 m wide (Fig. 4b),
378 to complex networks. In some cases they show also an polygonal patterns extending over
379 distances of a few meters (Fig. 4c). Observations using the TC-MC indicated that most of the
380 bacterial mat patches are very thin, forming layers ~1–2 mm thick. Microbial mats usually
381 comprise a mixture of taxa, with biomass dominated by large filamentous sulphide-oxidizing
382 bacteria (Beggiatoa, Thioploca, Arcobacter, Thiothrix) (Levin, 2005). The larger, spatially
383 continuous mats are whitish with a dark grey border, which is indicative of sulfidic conditions in
384 the underlying sediments. This suggests active sulfate reduction dominated by AOM at the active
385 methane seeps (Fig. 4b).

386

387 *4.5 Gas hydrate, methane, and gas measurements*

388 Within both pockmarks, several fissures observed at the seafloor expose a thin (~ 2-3 cm) crust
389 of surface sediment cemented by gas hydrate layers (Fig. 7c) indicating that the sediment surface
390 is still within the gas hydrate stability zone. When near surface gas hydrate was first observed in
391 real-time images, we deployed the CAGE888 and CAGE895 markers for future monitoring (Fig.
392 1c) and collected cores of the gas hydrate pavement using the TC-MC. During the lift-off of the
393 TC-MC system from the seafloor, we observed both in real-time and, in high-resolution images
394 many gas hydrate pieces in the water column, which were dislodged from seafloor during coring
395 (Fig. 7b). The pieces of gas hydrate were 5-8 cm in diameter at one of the stations. The sediment
396 recovered in the TC-MC core (MC893, Figure 1c) at the CAGE888 site also contained laminar
397 (3 to 5 mm) and nodular (2-3 cm) gas hydrate in the upper 10 cm of the core. On deck, gas

hydrate dissociation was intense, and bubbling occurred for ~30 minutes following recovery of all 5 of the TC-MC cores from the Lomvi pockmark (Panieri et al., 2015). Analyses of the uppermost sediment by the headspace technique yield a methane concentration of 5 mM (3×10^5 ppmv). Saturation of methane with respect to gas hydrate calculated using the phase prediction program CSMGem1 is 59.7 mM. Our methane values below saturation reflect extensive degassing of the core as evidenced by the intense bubbling observed.

We complement our data set on gas concentration and its isotopic composition at the Vestnesa seeps, with published and unpublished data from other sediment cores collected in Lomvi and Lunde during various cruises (CAGE13 and CAGE15-2, Table 1; Table 1SD).

All these cores were composed of mud, and were observed to expand and bubble profusely upon recovery. On deck, numerous gas filled gaps developed within the cores, and strong hydrogen sulfide scent was noted. Some of the core sections were observed to release gas for ~1 h after recovery. Such strong degassing results in the formation of a soupy, mousse-like fabric in the sediment, characteristic of gas expansion and gas hydrate dissociation (Paull and Ussler, 2001; Piñero et al., 2007). White veins ~2 cm thick and pieces of gas hydrate up to 10 cm in diameter were observed in many of the cores retrieved from the area.

A compilation of published and unpublished data from these cores ("head space gas" in Tables 2, Fig. 8) show that the gas is composed of ca 99% methane with a $\delta^{13}C$ isotopic range between −44.8 and −62.9‰ VPDB, and δD values from −140 to −229‰ VSMOW. The samples of gas hydrate ("gas hydrate" in Table 2) have a methane $\delta^{13}C$ average value of ca 51.4‰ VPDB (Fig. 8).

5. Discussion

5.1. Gas sources in Lomvi and Lunde

Smith et al. (2014) previously suggested that the gas hydrate system at Vestnesa is fed predominantly by thermogenic methane sources. Results from the head-space gas samples we report here indicate both microbial and thermogenic gas sources, with a predominantly mixed gas signature of the methane in both of the pockmarks studied (Figs. 8 and 9). Both gas sources can be expected in this environment, where at least 11 million years of sedimentation have resulted in a very thick (>2 km) accumulation of sediment (Mattingsdal et al., 2014). Thermogenic gas–producing source rocks exist in older Miocene-age sediments (Knies and Mann, 2002) recovered from ODP Site 909 ~50 km west of Vestnesa and apparently also exist in the equivalent-age sediments beneath the ridge (Dumke et al., 2016). Shallow microbial gas production occurs throughout the Vestnesa Ridge region as well, where sufficient organic carbon drives sulfate reduction, and fuels methanogenesis in sediments along the crest of the ridge (Hong et al., 2016).

5.2. Gas leakage mechanism: diffuse vs. focused outflow at the seafloor

There is evidence for both diffuse and focused flow within the Lomvi and Lunde pockmarks, whereas the seafloor outside the pockmarks lacks bacterial mats, tubeworms and carbonate concretions suggesting that presently these areas experience no major methane emissions. The extensive areal distribution of bacterial mats and tubeworms at the seafloor of both pockmarks suggests that the entire area is experiencing a slow but pervasive release of methane, which we call diffuse flow, as has been documented elsewhere (Boetius and Wenzhöfer, 2013). This is in agreement with the structure of the seismic chimneys below the pockmarks, where acoustic anomalies are indicative of a distributed fluid advection regime across the full extent of the pockmark region. The presence of pits within the pockmarks, on the other hand, points to a more focused fluid flow with active release of gas as indicated by presence of flares in the water column above the pits. This inference is corroborated by high amplitude anomalies in the gas

chimney beneath Lomvi, which stack and align vertically, cutting across disrupted strata and terminating into the pits at the seafloor (Fig. 2f). The observed flares are produced by trains of bubbles that escape from small orifices a few centimetres in diameter and that we name bubbling sites. These discrete locations in the pits move in space and time, but we estimate that at any given time they occupy ca 10 % of the pit floor (Table 3; Fig. 9).

The alignment of amplitude anomalies points towards a migration pathway via a specific self-enhanced and complex fracture system likely driven by fluid overpressures at depth (Cartwright et al., 2007; Hustoft et al., 2007). Deviation of the pathways away from the main upflow zone might be simply due to overburden stress or alternatively may result from permeability variations in the sediment, linked to hydrate formation clogging the fracture network (Liu and Flemings, 2007; Smith et al., 2014). Once a pathway to the seafloor exists, it could be sustained over a longer period of time, leading to the development of the small pits from where gas seeps into the ocean (Figs. 2c, f, and 9). The flanks of the pits and their immediate surrounding rims are steep, and likely reflect a slope break associated with outcrops of carbonate concretions and/or gas hydrates. While the main flux of gas likely happens along those pathways, this area may be surrounded by percolation at slow rates of expulsion leading to diffuse outflow at the seafloor over the larger perimeter of the main chimney. Such diffuse flow is evidenced by the areal distribution of bacterial mats and tubeworms and by widespread distribution of small carbonate concretions. The dense shell bed and MDAC nodules found at 1.5 mbsf in Lomvi, indicate that about 17,500 yrs BP, methane seepage sustained a chemosynthetic-based bivalve community for ca 1,000 yrs, also favouring carbonate precipitation (Ambrose et al., 2015). This suggests that methane emissions in Vestnesa are long-lived, but can be episodic with ~1ka temporal changes in both the magnitude of flow rates and fluid chemistry.

5.3 The fate of methane at Vestnesa Ridge

We show that the Lunde and Lomvi pockmarks are characterized by both diffuse and focused fluid outflow at the seafloor. Here we discuss the process of consumption of methane in the subseafloor via AOM, as this will impact the amount of methane carbon sequestered in authigenic carbonate, the flux of methane into the water column (including methane flares) and highlight differences between the two venting regimes. We note that within the pits there are several active bubbling sites that emit methane gas. Based on our hydroacoustic data analyses (see Supplementary data for details) we estimate that methane gas emanates from the pits within pockmarks at minimum rates ranging from 13 to 390 mmol m^{-2} d^{-1}, based on uncertainties in parameters, although the flux may be significantly higher. By assuming that 10% of the pit floor is actively bubbling at a given time, we arrive at a maximum estimate of 0.03 – 0.88 tons yr^{-1} of methane (Table 3). Because this methane is transported mainly in the gas phase at high flow rates it is not available for consumption by microbes (Luff et al., 2004). As postulated by these authors, when the pore water velocity is >90 cm yr^{-1}, fluids will bypass the benthic filter, break through the sediment surface, and deliver high amounts of methane into the bottom water. Thus we assume that microbial consumption of methane gas discharging within the pits is small relative to the overall methane flux, because the upward flow of methane-charged fluids at the pits is relatively high.

Visual surveys and cores retrieved from the area surrounding to the bubbling sites allows for estimates of the fraction of the total methane flux delivered from depth (as evidenced in the seismic data) that is consumed anaerobically by microbial communities. We currently don't have data on the uptake by aerobic methanotrophs above the Vestnesa Ridge pockmarks. Direct measurement of anaerobic methane oxidation performed at a location characterized by bacterial mats and siboglinid tubeworms around the pits yield a volumetric rate of 200 nmol cm^{-3} d^{-1} (T. Treude, unpubl. data). If we assume that the SMT has a thickness of 2 to 5 cm, we arrive at an integrated AOM rate of 1-10 mmol m^{-2} d^{-1} (Table 3). The AOM rate estimated by numerical

models at a similar setting is of 44 mmol m^{-2} d^{-1} (Table 3). These values have the same order of magnitude and are relatively similar given the variability expected in the highly heterogeneous environments around methane seepage. This extreme heterogeneity has been clearly documented in Hydrate Ridge (Torres et al., 2002; Sahling et al., 2002) and elsewhere. As a first approximation, acknowledging the uncertainties of these estimates, we arrive at a total methane sequestration as carbonates of 0.4 tons yr^{-1}

Away from the region that directly surrounds the bubbling pits, but still within the pockmark, the regime is diffusive and the emission of methane is very low. We do not have direct measurements in the diffusive region, but Hong et al. (2016) used a pore water modelling approach to calculate the diffusive output of methane and the fraction of this carbon trapped as carbonate. By assuming an AOM rate of 0.3 to 1.1 mmol m^{-2} d^{-1} they arrive at a methane flux estimate from Lomvi and Lunde that ranges from 1.1 to 4.9 tons yr^{-1}, and estimate that 0.3 to 1.2 tons of carbon per year is sequestrated in the authigenic carbonates (Table 3). When considered in the context of the large relative area of the pockmark that experiences this regime, carbonate formation in Lomvi and Lunde constitutes a substantial long-term methane carbon sink, consistent with an efficient removal of methane as carbonate via the microbial benthic filter (Niemann et al., 2006).

5.4 Seep community in Vestnesa Ridge pockmarks

Methane flux at the Vestnesa pockmarks sustains mats of sulfur-oxidizing bacteria, abundant siboglinid tubeworms (vestimentiferans and frenulates; see Rouse, 2001 for systematics of this group) dependant on endosymbiotic chemosynthetic bacteria (methanotrophs and/or thiotrophs) and few bivalves, which in our images often appear isolated and grazing on the seafloor. In addition, the methane-derived authigenic carbonates at the seafloor provide a hard substrate for

521 the establishment of dense communities of organisms that do not depend on chemosynthesis
522 (Levin et al., 2015).
523 Lunde and Lomvi methane seepage supports a high density of benthic life relative to the
524 surrounding areas, as observed in other Arctic seep locations (Åström et al., 2016). However the
525 lack of large size tubeworm, mussels and clams in the Vestnesa sites and in other high latitude
526 seep sites (Rybakova et al., 2013) differentiate these vents systems from those in mid and low
527 latitudes in the Atlantic and Pacific Oceans (e.g., Paull et al., 1984; Turnipseed et al., 2003;
528 Levin, 2005; Bernardino et al., 2012). Further work is required to elucidate why typical seep
529 communities dominated by large symbiont-bearing megafauna (vestimentiferan tube worms,
530 mytilid mussels, vesicomyid clams) are lacking in our study area and other high latitude
531 environments. More puzzling still is the observation of fossil chemosynthetic Vesicomydae
532 shells recovered in a core from this region, which provide evidence for abundant chemosynthetic
533 bivalve colonies ~17,500 yrs BP (Ambrose et al., 2015). Similar fossil assemblages have been
534 reported at extinct low-temperature vents associated with the Rainbow hydrothermal system that
535 is located off-axis from the Mid-Atlantic Ridge (Andreani et al., 2014; Lartaud et al., 2010;
536 2011). The Vesicomydae colonies reported by Ambrose et al. (2015) persisted for ca 1,000 yrs
537 until still unknown environmental changes may have led to the bivalve disappearance.
538 Episodicity of venting and discrete time intervals of bivalve colony development are not unusual
539 in seep environments; what is puzzling is the lack of large symbiont-bearing megafauna at
540 methane seeps located in modern-day high latitude regions.
541
542 *5.5. Formation and evolution of Vestnesa pockmarks*
543 Gas accumulation underneath the Vestnesa Ridge pockmarks is morphologically controlled
544 (Bünz et al., 2012) and the presence of faults and fractures that act as a pathway for fluid
545 migration, determine the chimney distribution underlying the pockmarks. This is true also for

546 Lunde and Lomvi, where the gas chimneys are directly linked to subsurface fault planes. The
547 chimneys extend from the base of the hydrate-stability zone up to the seafloor transporting
548 fluids, so that methane gas migrates in the subseafloor through the approximately 180-m-thick
549 gas hydrate stability zone (Hustoft et al., 2009; Bünz et al., 2012; Smith et al., 2014). Whether
550 the fluids are from the BSR or even deeper is difficult to determine given the thick free-gas zone
551 beneath the BSR that is masking the underlying layers beneath the GHSZ (Bünz et al., 2012).
552 Several lines of evidence suggest that fluid emissions in Lunde and Lomvi, and commonly in
553 other pockmarks along Vestnesa Ridge, are long-lived and periodically active.
554 The buried pockmarks or mounds mapped at various stratigraphic intervals and observations of
555 periods of inactivity indicate episodic seepage events (Plaza-Faverola et al., 2015), which have
556 been correlated with the onset and intensification of glaciations starting 2.7 Ma ago (Mattingsdal
557 et al., 2014). These seepage events last for few hundred thousand years and are related to glacial
558 intensification of the west Svalbard margin and fault reactivation and fracturing. Scattered blocks
559 of various size, pavements, and massive carbonate blocks observed within Lunde and Lomvi
560 testify for several cycles of carbonate precipitation or exhumation of carbonate indicating long-
561 lived seepage.
562 MDAC are common features at many pockmarks and seep sites along the Norwegian Margin
563 and in the Barents Sea (Hovland et al., 1987; Greinert et al., 2010; Haas et al., 2010; Bernardini
564 et al., 2016). Based on U-Th dating of MDAC, Crémière et al. (2016) developed a scenario for
565 the timing of past methane release events. According to these authors, retreat of Barents Sea ice
566 during the last deglaciation ca 20,000 years ago, destabilized gas hydrates and led to a vast
567 amount of methane release, with subsequent MDAC formation. Methane release continued for 7-
568 10,000 yr, tracking hydrate stability changes controlled by relative sea-level rise, bottom water
569 warming and fault reactivation from isostatic rebound (Crémière et al., 2016). We are not
570 advocating similar mechanisms for pockmark and MDAC formation in Vestnesa. While fluid

571 release and pockmark formation can be triggered by seafloor warming following ice retreat, the
572 pockmarks on Vestnesa Ridge are located in deep water where they are isolated from the effects
573 that bottom water temperature changes have at the upper limit of gas hydrate stability along the
574 Svalbard slope (Westbrook et al., 2009).
575 Collectively, these observations indicate that the formation and evolution of Lunde and Lomvi is
576 characterized by temporal changes in the magnitude of flow and most likely in the seep fluid
577 chemistry. Correlation with many pockmarks and seep sites along the Norwegian Margin and in
578 the Barents Sea (Hovland et al., 1987; Greinert et al., 2010; Haas et al., 2010; Mazzini et al.,
579 2016) we believe that that the evolution of the Vestnesa pockmarks is likely to be independent of
580 glacial-interglacial cyclicity, and rather it is linked to processes associated with the upwelling of
581 deeper methane-rich fluids, possibly thermogenic, and their expulsion at the seafloor.
582

583 **5.6 Comparison with other pockmark regions**

584 Pockmarks have been reported in many locations around the world in water depths ranging from
585 30 to 5000 m, i.e. from estuarine to abyssal plain settings (Hovland and Judd, 1988), and occur
586 in both random and non-random distribution patterns. The size of pockmarks can range from a
587 few meters to hundreds of meters in diameter, depending on the flux of fluid expulsion through
588 the shallow subsurface (e.g. Whiticar and Werner, 1981; Harrington, 1985; Hovland and Judd,
589 1988; Charlou et al., 2004). Pockmarks are the result of fluids (gas of thermogenic or biogenic
590 origin or aqueous fluid from rapidly buried and compacting sediments) migration though the
591 sedimentary column and expulsion at the seabed. There are various mechanisms postulated as
592 drivers for fluid advection, and include migration from overpressured reservoirs via tectonically
593 controlled such as faults and fractures, sediment compaction and overpressure dissipation via
594 fluid flow and mud diaper formation, salt-tectonic faulting, and gas hydrate dynamics. Gas
595 expulsion has been attributed to earthquake forcing.

596 Seafloor pockmarks were first reported along the sediment-water interface on the Scotian Shelf
597 by King and MacLean (1970) and since then they have received a lot of attention among the
598 scientific community because the seeping methane might contribute to the atmospheric
599 greenhouse gases, drive carbonate formation and support cold seep ecosystems hosting unique
600 fauna. Pockmarks may be common in petroleum basins and therefore of interest to the petroleum
601 industry.

602 A compilation of published data on pockmarks indicating water depth, mechanism and time of
603 formation, and seafloor characteristics such as the presence of chemosynthetic fauna and
604 carbonate formation is presented in Table 4. We note the preponderance of pockmarks in depths
605 shallower than the upper edge of gas hydrate stability; and note that although gas hydrate
606 destabilization has been postulated as a driving mechanisms for pockmarks reported in slope
607 margins, many of these inferences have not been confirmed by gas hydrate recovery. Pockmarks
608 occurring at greater depths (>1000 mbsf), which host gas hydrate deposits in the underlying
609 sediment, are not sensitive to environmentally-induced changes in gas hydrate stability, as
610 described here for the Vestnesa Ridge system. Whereas in some regions of the Arctic, such as
611 the Barents Sea, pockmark formation may be intimately tied to gas hydrate stability changes
612 associated with glacial/interglacial changes (Crémière et al., 2016), it is likely that these
613 represent a small fraction of the global pockmark occurrences. Rather, these features likely
614 reflect development of overpressures related to fluid (mostly gas) generation, tied to structural
615 changes in the overburden facility and channel gas migration to the seafloor. We also note that
616 although seafloor pockmarks are common along continental margins worldwide, and are
617 associated with gas advection from depth, there is a marked dearth of data on the effect of the
618 methane migration/discharge on carbon budgets. Except for methane expulsion rates (2.3 mm/a
619 Chaduteau et al., 2009) reported from the Regab pockmark (Congo margin) (Marcon et al.,
620 2014), ours is the only location among those listed in Table 4, from which methane discharge

621 rates and carbon sequestration budgets have been estimated. We acknowledge the uncertainties
622 in our estimates and the challenges in generating such data, but argue that it is important to
623 evaluate, at least to a first order approximation, the role of pockmark regions in the overall ocean
624 carbon budgets.

625

626 **6. Conclusions**

627 We present the first high-resolution deep-sea camera images showing carbonate formation at
628 seafloor pockmarks along the 1200 m deep and 100 km long crest of the Vestnesa Ridge,
629 specifically in two of the most active pockmarks, Lomvi and Lunde. Widespread authigenic
630 carbonates were observed only inside pockmarks, consistent with gas migration being channelled
631 within discrete regions imaged as acoustic chimneys underlying seafloor pockmarks. Integration
632 and synthesis of seismic data, real-time visual observations and TV-guided sampling permit us to
633 identify the ongoing diffuse and focused fluid flow regimes in Lomvi and Lunde.
634 Focused fluid flow is evidenced by major acoustic flares that image gas bubbles rising to ~800 m
635 above the seafloor. Methane discharge stems from the well-defined pits within the pockmarks.
636 The focused fluid flow sites are characterized by high amplitudes in the high-resolution 3D
637 seismic data, gas hydrate recovery from sediment cores and seafloor observations of extensive
638 bacterial mats. We estimate the free gas methane flux of individual gas flare observations at
639 bubbling sites in the pits to be at least on the order of 0.03 to 0.88 tons yr^{-1}, resulting in a water
640 column methane flux of 13 to 390 mmol m^{-2} d^{-1}, but we acknowledge uncertainties in this
641 estimate associated with the formation of hydrate skins not considered in our model. Diffuse
642 methane venting within the entirety of the pockmark is evidenced from core data. Using
643 published values for total AOM consumption, we estimate the methane sequestration through
644 authigenic carbonate formation from the two pockmarks to be in the order of 1.1 to 4.9 tons yr^{-1},
645 which represents a large sink for methane-carbon.

The discovery of extensive authigenic carbonate outcrops on the seafloor within pockmarks at Vestnesa Ridge, together with estimates of carbon sequestration by the MDAC, has important implications for understanding gas hydrate formation, dissociation and gas release in the Arctic Ocean. Authigenic carbonates associated with cold seeps provide valuable archives of changes in long-term seep activity, with the potential to constrain times of activity and carbonate precipitation rates.

ACKNOWLEDGMENTS

This work was supported by the Research Council of Norway through its Centre of Excellence funding scheme for CAGE, project number 223259. We thank Jürgen Mienert, Jochen Knies, and Matthias Forwick for useful discussions, Tine Treude who provide direct measurement of anaerobic methane oxidation in Vestensa Ridge, Andrew Thurber who assisted with the identification of fauna in the seafloor images, two anonymous reviewers and the Editor Gert J. De Lange for useful suggestions. We thank all the members of the cruises scientific party, and the captain, and crewmembers of *R/V Helmer Hanssen* during the 2013 and 2015 expeditions. Special thanks to Marshall Swartz of WHOI who assisted in the mobilization and testing of the TC-MC system for this work; Kevin Manganini at WHOI for assistance in the mechanical design of the TC-MS system; and Bjørn Runar Olsen and Steinar Iversen for support during shipboard operations. D. J. Fornari was supported by WHOI's Investment in Science Fund and the US National Science Foundation grant OCE1154266. J. Escartin was partially supported by the Deep Carbon Observatory initiative awarded by the Alfred P. Sloan Foundation. M. Torres acknowledges support from the US Department of Energy (grant DE-FE0013531) and a fellowship from the Hanse Wissenschaftkollege (Germany). We also acknowledge software support from Schlumberger, DECO Geophysical.

671 **Reference**

672 Abrams, M., 1992. Geophysical and geochemical evidence for subsurface hydrocarbon leakage
673 in the Bering Sea, Alaska. Marine and Petroleum Geology 9, 208–221.
674 Aloisi, G., Bouloubassi, I., Heijs, S.K., Pancost, R.D., Pierre, C., Sinninghe Damsté, J.S.,
675 Gottschal, J.C., Forney, L.J., Rouchy, J.-M., 2002. CH_4-consuming microorganisms and the
676 formation of carbonate crusts at cold seeps. Earth and Planetary Science Letters 203, 195-203.
677 Aloisi, G., Pierre, C., Rouchy, J.-M., Foucher, J.-P., Woodside, J., 2000. Methane-related
678 authigenic carbonates of eastern Mediterranean Sea mud volcanoes and their possible relation to
679 gas hydrate destabilisation. Earth and Planetary Science Letters 184, 321-338.
680 Ambrose, W.G., Panieri, G., Schneider, A., Plaza-Faverola, A., Carroll, M.L., Åström, E.K.L.,
681 Locke, W.L., Carroll, J., 2015. Bivalve shell horizons in seafloor pockmarks of the last glacial-
682 interglacial transition: a thousand years of methane emissions in the Arctic Ocean.
683 Geochemistry, Geophysics, Geosystems 16, 4108-4129.

684 Andreani, M., Escartín, J., Delacour, A., Ildefonse, B., Godard, M., Dyment, J., Fallick, A.E.,
685 and Fouquet, Y., 2014. Tectonic structure, lithology, and hydrothermal signature of the Rainbow
686 mas- sif (Mid-Atlantic Ridge 36°14′N): Geochemistry, Geophysics, Geosystems 15, 3543-3571,
687 doi:10.1002/2014GC005269.

688 Åström, E.K.L., Carroll, M.L., Ambrose, W.G., Jr., Carroll, J., 2016. Arctic cold seeps in marine
689 methane hydrate environments: impacts on shelf macrobenthic community structure offshore
690 Svalbard. Marine Ecology Progress Series 552, 1-18.
691 Bayon, G., Dupre, S., Ponzevera, E., Etoubleau, J., Cheron, S., Pierre, C., Mascle, J., Boetius, A.,
692 de Lange, G.J., 2013. Formation of carbonate chimneys in the Mediterranean Sea linked to deep-
693 water oxygen depletion. Nature Geosciences 6, 755-760.

694 Baraza, J., Ercilla, G., 1996. Gas-charged sediments and large pockmark-like features on the
695 Gulf of Cadiz slope (SW Spain). Marine and Petroleum Geology, 3(2), 253- 261.

696 Barrie, V.J., Cook, S., Conway, K.W., 2011. Cold seeps and benthic habitat on the Pacific
697 margin of Canada. Continental Shelf Research 31, S85–S92.
698 Bernard, B.B., Brooks, J.M., Sackett, W.M., 1978. Light hydrocarbons in recent Texas
699 continental shelf and slope sediments. Journal of Geophysical Research: Oceans 83, 4053-4061.
700 Bernardino, A.F., Levin, L.A., Thurber, A.R., Smith, C.R., 2012. Comparative Composition,
701 Diversity and Trophic Ecology of Sediment Macrofauna at Vents, Seeps and Organic Falls.
702 PLoS ONE 7, e33515.
703 Boetius, A., Ravenschlag, K., Schubert, C. J., Rickert, D., Widdel, F., Gieske, A., Amann, R.,
704 Jørgensen, B.B., Witte, U., Pfannkuche, O., 2000. A marine anaerobic consortium apparently
705 mediating anaerobic oxidation of methane. Nature 407, 623–626.
706 Boetius, A., Wenzhofer, F., 2013. Seafloor oxygen consumption fuelled by methane from cold
707 seeps. Nature Geosciences 6, 725-734.
708 Bünz, S., Polyanov, S., Vadakkepuliyambatta, S., Consolaro, C., Mienert, J., 2012. Active gas
709 venting through hydrate-bearing sediments on the Vestnesa Ridge, offshore W-Svalbard. Marine
710 Geology 332-334, 189-197.
711 Cartwright, J., Huuse, M., Aplin, A., 2007. Seal bypass systems. AAPG Bulletin 91, 1141-1166.
712 Casas, D., Ercilla, G., Baraza, J., 2003. Acoustic evidences of gas in the continental slope
713 sediments of the Gulf of Cadiz (E Atlantic). Geo-Marine Letters 23, 300–310.

714 Chaduteau, C., Jean-Baptiste, P., Fourré, E., Charlou, J.L., Donval, J.P., 2009, Helium transport
715 in sediment pore fluids of the Congo-Angola margin: Geochemistry Geophysics Geosystems 10.
716 Q01002, doi:10.1029/2007GC001897.

717 Chand, S., Rise, L., Ottesen, D., Dolan, M.F.J., Bellec, V., Bøe, R., 2009. Pockmark-like
718 depressions near the Goliat hydrocarbon field, Barents Sea: Morphology and genesis. Marine
719 and Petroleum Geology 26, 1035-1042.

720 Charlou, J.L., Donval, J.P., Fouquet, Y., Ondréas, H., Knoery, J., Cochonat, P., Levaché, D.,
721 Poirier, Y., Jean-Baptiste, P., Fourré, E., Chazallon, B., 2004. Physical and chemical
722 characterization of gas hydrates and associated methane plumes in the Congo–Angola Basin.
723 Chemical Geology 205, 405-425. doi:10.1016/j.chemgeo.2003.12.033.

724 Chen, J., Song, H., Guan, Y., Yang, S., Pinheiro, L.M., Bai, Y., Liu, B., Geng, M., 2015.
725 Morphologies, classification and genesis of pockmarks, mud volcanoes and associated fluid
726 escape features in the northern Zhongjiannan Basin, South ChinaSea. Deep-Sea Research II 122,
727 106–117.

728 Christodoulou, D., Papatheodorou, G., Ferentinos, G., Masson, M., 2003. Active seepage in two
729 contrasting pockmark fields in the Patras and Corinth gulfs, Greece. Geo-Marine Letter 23, 194–
730 199
731 Clayton, C., 1991. Carbon isotope fractionation during natural gas generation from kerogen.
732 Marine and Petroleum Geology 8, 232-240.
733 Crémière, A., Bayon, G., Ponzevera, E., Pierre, C., 2013. Paleo-environmental controls on cold
734 seep carbonate authigenesis in the Sea of Marmara. Earth and Planetary Science Letters 376,
735 200-211.
736 Crémière, A., Lepland, A., Chand, S., Sahy, D., Condon, D.J., Noble, S.R., Martma, T.,
737 Thorsnes, T., Sauer, S., Brunstad, H., 2016. Timescales of methane seepage on the Norwegian
738 margin following collapse of the Scandinavian Ice Sheet. Nat Communication 7, 11509.
739 doi:10.1038/ncomms11509.

De Mahiques, M.M., Schattner, U., Lazar, M., Sumida, P.Y.G., de Souza, L.A.P., 2017. An extensive pockmark field on the upper Atlantic margin of Southeast Brazil: spatial analysis and its relationship with salt diapirism. Heliyon, 3(2), e00257. http://doi.org/10.1016/j.heliyon.2017.e00257

Dumke, I., Burwicz, E.B., Berndt, C., Klaeschen, D., Feseker, T., Geissler, W.H., Sarkar, S., 2016. Gas hydrate distribution and hydrocarbon maturation north of the Knipovich Ridge, western Svalbard margin. Journal of Geophysical Research: Solid Earth 121, 1405-1424.

Eiken, O., Hinz, K., 1993. Contourites in the Fram Strait. Sedimentary Geology 82, 15-32.

Engen, Ø., Faleide, J.I., Dyreng, T.K., 2008. Opening of the Fram Strait gateway: A review of plate tectonic constraints. Tectonophysics 450, 51-69.

Ergün, M., Dondurur, D., Cifçi, G., 2002. Acoustic evidence for shallow gas accumulations in the sediments of the Eastern Black Sea. Terra Nova 14, 313–320.

Fornari, D.J., Group, W.T., 2003. A new deep-sea towed digital camera and multi-rock coring system. Eos, Transactions American Geophysical Union 84, 69-73.

Forsberg, C., Plank, S., Tjelta, T., Svano, G., Strout, J., Svensen, H., 2007. Formation of pockmarks in the Norwegian Channel, Offshore site investigation and geotechnics, Confronting New Challenges and Sharing Knowledge. 11-13 september 2007. Society of Underwater Technology, SUT-OSIG-07-221.

Forwick, M., Baeten, N.J., Vorren,T.O., 2009. Pockmarks in Spitsbergenfjords. Norwegian Journal of Geology 89,65-77.

Garcia-Garcia, A., Orange, D.L., Maher, N.M., Heffernan, A.S., Fortier, G.S., Malone, A., 2004. Geophysical evidence for gas geohazards off Iskenderun Bay, SE Turkey. Marine and Petroleum Geology 21, 1255–1264.

763 Greinert, J., 2008. Monitoring temporal variability of bubble release at seeps: The hydroacoustic
764 swath system GasQuant. Journal of Geophysical Research 113, C07048,
765 doi:10.1029/2007JC004704.
766 Greinert, J., Artemov, Y., Egorov, V., De Batist, M., McGinnis, D., 2006. 1300-m-high rising
767 bubbles from mud volcanoes at 2080 m in the Black Sea: Hydroacoustic characteristics and
768 temporal variability. Earth and Planetary Science Letters 244, 1-15.
769 Greinert, J., Lewis, K.B., Bialas, J., Pecher, I.A., Rowden, A., Bowden, D.A., De Batist, M.,
770 Linke, P., 2010. Methane seepage along the Hikurangi Margin, New Zealand: overview of
771 studies in 2006 and 2007 and new evidence from visual, bathymetric and hydroacoustic
772 investigations. Mar. Geol. 272 (1–4), 6–25.

773 Haas, A., Peckmann, J., Elvert, M., Sahling, H., Bohrmann, G., 2010. Patterns of carbonate
774 authigenesis at the Kouilou pockmarks on the Congo deep-sea fan. Mar. Geol. 268 (1–4), 129–
775 136.

776 Halliday, E.J. Barrie, J.V. Chapman N.R., Rohr, K.M.M., 2008. Structurally controlled
777 hydrocarbon seeps on a glaciated continental margin, Hecate Strait, offshore British Columbia.
778 Marine Geology 252, 193–206

779 Harrington, P., 1985. Formation of pockmarks by pore-water escape. Geo-Marine Letters 5, 193-
780 197.

781 Hasiotis, T. Papatheodorou, G. Kastanos, N. Ferentinos G., 1996. A pockmark field in the Patras
782 Gulf (Greece) and its activation during the 14/7/93 seismic event. Marine Geology 130, 333–
783 344.

784 Hilário, A., Capa, M., Dahlgren, T.G., Halanych, K.M., Little, C.T.S., Thornhill, D.J., Verna, C.,
785 Glover, A.G., 2011. New Perspectives on the Ecology and Evolution of Siboglinid Tubeworms.
786 PLoS ONE 6, e16309.
787 Hoehler, T.M., Borowski, W.S., Alperin, M.J., Rodriguez, N.M., Paull, C.K., 2000. Model,
788 stable isotope, and radiotracer characterization of anaerobic methane oxidation in gas hydrate-
789 bearing sediments of the Blake Ridge, Proceedings of the Ocean Drilling Program, Scientific
790 Results. Ocean Drilling Program College Station, TX, pp. 79-85.
791 Hong, W.-L., Sauer, S., Panieri, G., Ambrose, W.G., James, R.H., Plaza-Faverola, A., Schneider,
792 A., 2016. Removal of methane through hydrological, microbial, and geochemical processes in
793 the shallow sediments of pockmarks along eastern Vestnesa Ridge (Svalbard). Limnology and
794 Oceanography, 61: S324–S343. doi:10.1002/lno.10299.
795 Hovland, M., 1981. A classification of pockmark related features in the Norwegian Trench.
796 Institutt for kontinentalsokkelundersøkelser . Continental Shelf Institute, 106.
797 Hovland, M., 1985. Seabed Features Caused by Shallow Gas in North Sea. AAAPG Bulletin 69,
798 267-267.
799 Hovland, M., 1991. Large pockmarks, gas-charged sediments and possible clay diapirs in the
800 Skagerrak, Marine and Petroleum Geology 8 (3), 311-316, ISSN 0264-8172,
801 http://dx.doi.org/10.1016/0264-8172(91)90085-F.
802 Hovland, M., Heggland, R., De Vries, M.H., Tjelta, T.I., 2010. Unit-pockmarks and their
803 potential significance for predicting fluid flow, Marine and Petroleum Geology 27 (6), 1190-
804 1199, https://doi.org/10.1016/j.marpetgeo.2010.02.005.

805 Hovland, M., Judd, A., 1988. Seabed pockmarks and seepages: impact on geology, biology, and
806 the marine environment. Graham and Trotman.

807 Hovland, M., Talbot, M.R., Qvale, H., Olaussen, S., Aasberg, L., 1987. Methane-related
808 carbonate cements in pockmarks of the North Sea. J. Sediment. Petrol. 57 (5), 881–892.

809 Howe, J.A., Shimmield, T.M., Harland, R.E.X., Eyles, N., 2008. Late Quaternary contourites and
810 glaciomarine sedimentation in the Fram Strait. Sedimentology 55, 179-200.
811 Hustoft, S., Bünz, S., Mienert, J., Chand, S., 2009. Gas hydrate reservoir and active methane-
812 venting province in sediments on < 20 Ma young oceanic crust in the Fram Strait, offshore
813 NW-Svalbard. Earth and Planetary Science Letters 284, 12-24.
814 Hustoft, S., Mienert, J., Bünz, S., Nouzé, H., 2007. High-resolution 3D-seismic data indicate
815 focussed fluid migration pathways above polygonal fault systems of the mid-Norwegian margin.
816 Marine Geology 245, 89-106.
817 Ingrassia, M., Martorelli, E., Bosman, A., Macelloni, L., Sposato, A., Chiocci, F.L., 2015. The
818 Zannone Giant Pockmark: First evidence of a giant complex seeping structure in shallow-water,
819 central Mediterranean Sea, Italy. Marine Geology 363, 38-51,
820 doi.org/10.1016/j.margeo.2015.02.005.
821 Johnson, J.E., Mienert, J., Plaza-Faverola, A., Vadakkepuliyambatta, S., Knies, J., Bünz, S.,
822 Andreassen, K., Ferré, B., 2015. Abiotic methane from ultraslow-spreading ridges can charge
823 Arctic gas hydrates. Geology 43, 371-374, doi:10.1130/G36440.1
824 Judd, A., Hovland, M., 2007. Seabed fluid flow: the impact on geology, biology and the marine
825 environment. Cambridge University Press, p. 475.
826 Karisiddaiah, S.M. Veerayya M., 2002. Occurrence of pockmarks and gas seepages along the
827 central western continental margin of India. Curr. Sci. 82, 52–57
828 Kelley, J.T., Dickson, S.M., Belknap, D.F., Barnhardt, W.A., Henderson, M., 1994. Giant sea-
829 bed pockmarks: evidence for gas escape from Belfast Bay, Maine. Geology 22, 59–62.

King, L.H., MacLean, B., 1970, Pockmarks on the Scotian Shelf. Geological Society of America Bulletin 81, 3141–3148. doi:10.1130/00167606(1970)81[3141:POTSS]2.0.CO;2.

Knies, J., Mann, U., 2002. Depositional environment and source rock potential of Miocene strata from the central Fram Strait: introduction of a new computing tool for simulating organic facies variations. Marine and Petroleum Geology 19, 811-828.

Knies, J., Matthiessen, J., Vogt, C., Laberg, J.S., Hjelstuen, B.O., Smelror, M., Larsen, E., Andreassen, K., Eidvin, T., Vorren, T.O., 2009. The Plio-Pleistocene glaciation of the Barents Sea–Svalbard region: a new model based on revised chronostratigraphy. Quaternary Science Reviews 28, 812-829.

Lartaud, F., et al., 2010, Fossil clams from a serpentinite-hosted sedimented vent field near the active smoker complex Rainbow, MAR, 36°13′N: Insight into the biogeography of vent fauna: Geochemistry, Geophysics, Geosystems 11, Q0AE01, doi:10.1029/2010GC003079.

Leifer, I., Patro, R.K., 2002. The bubble mechanism for methane transport from the shallow sea bed to the surface: A review and sensitivity study. Continental Shelf Research 22, 2409-2428.

Leifer, I., Patro, R.K., Bowyer, P., 2000. A study on the temperature variation of rise velocity for large clean bubbles. Journal of Atmospheric and Oceanic Technology 17, 1392-1402.

Levin, L.A., 2005. Ecology of cold seep sediments: interactions of fauna with flow, chemistry and microbes. Oceanography and Marine Biology: an annual review 43, 1-46.

Levin, L.A., Mendoza, G.F., Grupe, B.M., Gonzalez, J.P., Jellison, B., Rouse, G., Thurber, A.R., Waren, A., 2015. Biodiversity on the rocks: macrofauna inhabiting authigenic carbonate at Costa Rica methane seeps. PLoS ONE 10, e0131080.

Liu, X., Flemings, P.B., 2007. Dynamic multiphase flow model of hydrate formation in marine sediments. Journal of Geophysical Research, 112, B03101, doi:10.1029/2005JB004227.

853 Luff, R., Wallmann, K., Aloisi, G., 2004. Numerical modeling of carbonate crust formation at
854 cold vent sites: significance for fluid and methane budgets and chemosynthetic biological
855 communities. Earth and Planetary Science Letters 221, 337-353.
856 Long, D., 1992. Devensian late-glacial gas escape in the central North Sea. Continental Shelf
857 Research 12, 1097-1110. http://dx.doi.org/10.1016/0278-4343(92)90071-Q.
858 Løseth, H., Gading, M., Wensaas, L., 2009. Hydrocarbon leakage interpreted on seismic data.
859 Marine and Petroleum Geology 26, 1304-1319.
860 Maksimov, A.O., 2005. Maximum size of a gas bubble in the regime of automodel pulsation.
861 Technical Physics Letters 31, 270-273.
862 Marcon, Y. and Ondréas, H., Sahling, H., Bohrmann, G., Olu, K., 2014. Fluid flow regimes and
863 growth of a giant pockmark. Geology, G34801.1, fdoi:10.1130/G34801.1
864 Mattingsdal, R., Knies, J., Andreassen, K., Fabian, K., Husum, K., Grøsfjeld, K., De Schepper,
865 S., 2014. A new 6 Myr stratigraphic framework for the Atlantic–Arctic Gateway. Quaternary
866 Science Reviews 92, 170-178.

867 Mazzini, A., Svensen, H.H., Forsberg, C.F., Linge, H., Lauritzen, S.-E., Haflidason, H.,
868 Hammer, Ø., Planke, S., Tjelta, T.I., 2017. A climatic trigger for the giant Troll pockmark field
869 in the northern North Sea. Earth and Planetary Science Letters, 464, 24-34.
870 doi.org/10.1016/j.epsl.2017.02.014.

871 Mazzini, A., Svensen, H.H., Planke, S. Forsberg, C.F., Tjelta, T.I., 2016. Pockmarks and
872 methanogenic carbonates above the giant Troll gas field in the Norwegian North Sea. Marine
873 Geology 373, 26–38.
874 McGinnis, D.F., Greinert, J., Artemov, Y., Beaubien, S., Wüest, A., 2006. Fate of rising methane
875 bubbles in stratified waters: How much methane reaches the atmosphere? Journal of Geophysical
876 Research: Oceans 111.

877 Medwin, H., Clay, C.S., 1997. Fundamentals of acoustical oceanography. Academic Press.
878 Mendelson, H.D., 1967. The prediction of bubble terminal velocities from wave theory. AIChE
879 Journal 13, 250-253.
880 Mienert, J., Posewang, J., Baumann, M., 1998. Gas hydrates along the northeastern Atlantic
881 margin: possible hydrate-bound margin instabilities and possible release of methane. In: J.P.
882 Henriet, J. Mienert (Eds.), Gas Hydrates: Relevance to World Margin Stability and Climate
883 Change, Geological Society, London, Special Publication 137, 275–291.
884 Muyakshin, S., Sauter, E., 2010. The hydroacoustic method for the quantification of the gas flux
885 from a submersed bubble plume. Oceanology 50, 995-1001.
886 Naudts, L., Greinert, J., Artemov, Y., Beaubien, S.E., Borowski, C., De Batist, M., 2008.
887 Anomalous sea-floor backscatter patterns in methane venting areas, Dnepr paleo-delta, NW
888 Black Sea, Marine Geology 251 (3–4), 253-267, https://doi.org/10.1016/j.margeo.2008.03.002.
889 Naudts, L., Greinert, J., Artemov, Y., Staelens, P., Poort, J., Van Rensbergen, P., De Batist, M.,
890 2006. Geological and morphological setting of 2778 methane seeps in the Dnepr paleo-delta,
891 northwestern Black Sea. Marine Geology 227, 177-199.
892 Niemann, H., Losekann, T., de Beer, D., Elvert, M., Nadalig, T., Knittel, K., Amann, R., Sauter,
893 E.J., Schluter, M., Klages, M., Foucher, J.P., Boetius, A., 2006. Novel microbial communities of
894 the Haakon Mosby mud volcano and their role as a methane sink. Nature 443, 854-858.
895 Ona, E., 1999. Methodology for target strength measurements. ICES Cooperative Research
896 Report 235, 59 pp.

897 O´Regan M.,Forwick, M., Jakobsson, M., Moran, K., Mocher, D., 2015. Sea floor cratering and
898 sediment remolding at sites of fluid escape. Geology 43, 895-898. doi:10.1130/G36945.1.

899 Panieri, G., Fornari, D.J., Serov, P., Åström, E. K. L., Plaza-Faverola, A., Mienert, J., Torres,
900 M.E., 2015. Gas Hydrate, Carbonate Crusts, and Chemosynthetic Organisms on a Vestnesa
901 Ridge Pockmark-Preliminary Findings. Fire in the ice 15, 14-17.
902 Partyka, G., Gridley, J., Lopez, J., 1999. Interpretational applications of spectral decomposition
903 in reservoir characterization. The Leading Edge 18, 353-360.
904 Pau, M., Gisler, G., Hammer, Ø., 2014. Experimental investigation of the hydrodynamics in
905 pockmarks using particle tracking velocimetry. Geo-Marine Letters 34, 11-19.
906 Pau M., Hammer Ø., Chand S., 2014. Constraints on the dynamics of pockmarks in the SW
907 Barents Sea: evidence from gravity coring and high-resolution, shallow seismic profiles. Marine
908 Geology 355, 330–345.
909 Paull, C., Hecker, B., Commeau, R., Freeman-Lynde, R., Neumann, C., Corso, W., Golubic, S.,
910 Hook, J., Sikes, E., Curray, J., 1984. Biological communities at the Florida Escarpment resemble
911 hydrothermal vent taxa. Science 226, 965-967.
912 Paull, C.K., Ussler, W., 2001. History and Significance of Gas Sampling During DSDP and ODP
913 Drilling Associated with Gas Hydrates, Natural Gas Hydrates: Occurrence, Distribution, and
914 Detection. American Geophysical Union, pp. 53-65.
915 Paull, C., Ussler III, W., Maher, N., Greene, H.G., Rehder, G., Lorenson, T., Lee, H., 2002.
916 Pockmarks off Big Sur, California. Marine Geology 181 (4), 323-335. doi.org/10.1016/S0025-
917 3227(01)00247-X.
918 Peckmann, J., Reimer, A., Luth, U., Luth, C., Hansen, B.T., Heinicke, C., Hoefs, J., Reitner, J.,
919 2001. Methane-derived carbonates and authigenic pyrite from the northwestern Black Sea.
920 Marine Geology 177, 129-150.
921 Piñero, E., Gràcia, E., Martínez-Ruiz, F., Larrasoaña, J.C., Vizcaino, A., Ercilla, G., 2007. Gas
922 hydrate disturbance fabrics of southern Hydrate Ridge sediments (ODP Leg 204): Relationship
923 with texture and physical properties. Geo-Marine Letters 27, 279-288.

924 Planke, S., Eriksen, F.N., Berndt, C., Mienert, J., Masson, D., 2009. P-Cable high-resolution
925 seismic. Oceanography 22, 85.
926 Plaza-Faverola, A., Bünz, S., Johnson, J.E., Chand, S., Knies, J., Mienert, J., Franek, P., 2015.
927 Role of tectonic stress in seepage evolution along the gas hydrate-charged Vestnesa Ridge, Fram
928 Strait. Geophysical Research Letters 42, 733-742.
929 Plaza-Faverola, A., S. Bünz, and J. Mienert (2010), Fluid distributions inferred from P-wave
930 velocity and reflection seismic amplitude anomalies beneath the Nyegga pockmark field of the
931 mid-Norwegian margin. Marine and Petroleum Geology 27(1), 46–60.
932 Prados, R., Garcia, R., Neumann, L., 2014. Image Blending Techniques and Their Application in
933 Underwater Mosaicing. Springer International Publishing107 pp. 10.1007/978-3-319-05558-9
934 Rice, D.D., Claypool, G.E., 1981. Generation, accumulation, and resource potential of biogenic
935 gas. AAPG Bulletin 65, 5-25.
936 Rollet, N. Logan, G.A. Kennard, J.M. O'Brien, P.E. Jones, A.T. Sexton M., 2006.
937 Characterization and correlation of active hydrocarbon seepage using geophysical data sets: an
938 example from the tropical, carbonate Yampi Shelf, Northwest Australia. Marine and Petroleum
939 Geology 23,145–164.
940 Römer, M., Sahling, H., Pape, T., Bahr, A., Feseker, T., Wintersteller, P., Bohrmann, G., 2012.
941 Geological control and quantity of methane ebullition from a high-flux seep area in the Black
942 Sea - the Kerch seep area. Marine Geology 319-322, 57-74. doi: 10.1016/j.margeo.2012.07.005.
943 Rouse, G.W., 2001. A cladistic analysis of Siboglinidae Caullery, 1914 (Polychaeta, Annelida):
944 formerly the phyla Pogonophora and Vestimentifera. Zoological Journal of the Linnean Society
945 132, 55-80.
946 Rybakova, E., Galkin, S., Bergmann, M., Soltwedel, T., Gebruk, A., 2013. Density and
947 distribution of megafauna at the Håkon Mosby mud volcano (the Barents Sea) based on image
948 analysis. Biogeosciences 10, 3359-3374.

949 Sassen, R., Losh, S., Cathles, L., Roberts, H.H., J.K Whelan, J.K. A.V Milkov, A.V., Sweet, S.T
950 DeFreitas, D.A , 2001. Massive vein-filling gas hydrate: Relation to ongoing gas migration from
951 the deep subsurface Gulf of Mexico. Marine and Petroleum Geology, 18, 551–560.
952 Sassen, R., Milkov, A.V. Roberts, H.H., Sweet, S.T., DeFreitas, D.A., 2003. Geochemical
953 evidence of rapid hydrocarbon venting from a seafloor-piercing mud diapir, Gulf of Mexico
954 continental shelf, Marine Geology 198 (3-4), 319-329. https://doi.org/10.1016/S0025-
955 3227(03)00121-X.
956 Sahling, H., Bohrmann, G., Artemov, Y.G., Bahr, A., Brüning, M., Klapp, S.A., Klaucke, I.,
957 Kozlova, E., Nikolovska, A., Pape, T., 2009. Vodyanitskii mud volcano, Sorokin trough, Black
958 Sea: Geological characterization and quantification of gas bubble streams. Marine and Petroleum
959 Geology 26, 1799-1811.
960 Sahling, H., Bohrmann, G., Spiess, V., Bialas, J., Breitzke, M., Ivanov, M., Kasten, S., Krastel,
961 S., Schneider, R., 2008. Pockmarks in the northern Congo fan area, SW Africa: Complex
962 seafloor features shaped by fluid flow. Marine Geology 249 (3–4), 206–225.
963 Sahling, H., Rickert, D., Lee, R.W., Linke, P., Suess, E., 2002. Macrofaunal community
964 structure and sulfide flux at gas hydrate deposits from the Cascadia convergent margin, NE
965 Pacific. Marine Ecology Progress Series 231, 121-138.
966 Sahling, H., Römer, M., Pape, T., Bergès, B., C. dos Santos Fereirra, C., Boelmann, J., Geprägs,
967 P., Tomczyk, M., Nowald, N., Dimmler, W., Schroedter, L., Glockzin, M., Bohrmann, G., 2014.
968 Gas emissions at the continental margin west of Svalbard: mapping, sampling, and
969 quantification. Biogeosciences 11, 6029–6046.
970 Shakhova, N., Semiletov, I., Leifer, I., Sergienko, V., Salyuk, A., Kosmach, D., Chernykh, D.,
971 Stubbs, C., Nicolsky, D., Tumskoy, V., Gustafsson, O., 2014. Ebullition and storm-induced
972 methane release from the East Siberian Arctic Shelf, Nature Geoscience, 7(1), 64–70,
973 doi:10.1038/ngeo2007.

974 Sibuet, M., Olu, K., 1998. Biogeography, biodiversity and fluid dependence of deep-sea cold-
975 seep communities at active and passive margins. Deep Sea Research Part II: Topical Studies in
976 Oceanography 45, 517-567.
977 Smith, A.J., Mienert, J., Bünz, S., Greinert, J., 2014. Thermogenic methane injection via bubble
978 transport into the upper Arctic Ocean from the hydrate-charged Vestnesa Ridge, Svalbard.
979 Geochemistry, Geophysics, Geosystems 15, 1945-1959.
980 Solheim, A., Elverhøi, A., 1985. A pockmark field in the Central Barents Sea; gas from a
981 petrogenic source? Polar Research 3 (new series), 11–19. http://dx.doi.org/10.1111/j.1751-
982 8369.1985.tb00492.x.
983 Solheim, A., Elverhøi, A., 1993. Gas-related sea floor craters in the Barents Sea. Geo-
984 Marine Letters 13, 235–243. http://dx.doi.org/10.1007/BF01207753.

985 Somoza, L., Diaz-del-Rio,V., Leon, R., Ivanov, M.K., Fenandez-Puga, M.C., Lobato, A.,
986 Maestro, A., Hernandez-Molina, F.J., Gardner, J.M., Rodero, J., Pinheiro, L.M., Vasquez, J.T.,
987 Medialdea, T., Fernandez-Salas, L.M., 2003. Seabed morphology and hydrocarbon seepage in
988 the the Gulf of Cadiz mud volcano area: imagery of multibeam data and ultra-high resolution
989 data. Marine Geology 195(1-4), 153-176.

990 Stoll, R.D., Ewing, J.I., Bryan, G.M., 1971. Anomalous wave velocities in sediments containing
991 gas hydrates. Journal of Geophysical Research 76, 2090-2094.
992 Sultan, N., Marsset, B. Ker, S., Marsset, T., Voisset, M., Vernant, A. M., Bayon, G., Cauquil, E.,
993 Adamy, J., Colliat, J. L., Drapeau, D., 2010. Hydrate dissolution as a potential mechanism for
994 pockmark formation in the Niger delta. Journal of Geophysical Research, 115, B08101,
995 doi:10.1029/2010JB007453.
996 Sumida, P.Y.G., Yoshinaga, Y.M., Saint-Pastous Madureira, L.A., Hovland, M., 2004. Seabed
997 pockmarks associated with deepwater corals off SE Brazilian continental slope, Santos Basin.

998 Marine Geology 207, 159–167.
999 Sun, Q., Wu, S., Hovland, M., Luo, P., Lu, Y., Qu, T., 2011. The morphologies and genesis of
1000 mega-pockmarks near the Xisha Uplift, South China Sea. Marine and Petroleum Geology
1001 28(6),146-1156. doi.org/10.1016/j.marpetgeo.2011.03.003.
1002 Taviani, M., 2001. Fluid venting and associated processes, in: Vai, G.B., Martini, I.P. (Eds.),
1003 Anatomy of an Orogen: the Apennines and Adjacent Mediterranean Basins. Springer
1004 Netherlands, Dordrecht, pp. 351-366.
1005 Torres, M., McManus, J., Hammond, D., De Angelis, M., Heeschen, K., Colbert, S., Tryon, M.,
1006 Brown, K., Suess, E., 2002. Fluid and chemical fluxes in and out of sediments hosting methane
1007 hydrate deposits on Hydrate Ridge, OR, I: Hydrological provinces. Earth and Planetary Science
1008 Letters 201, 525-540.
1009 Turnipseed, M., Knick, K.E., Lipcius, R.N., Dreyer, J., Van Dover, C.L., 2003. Diversity in
1010 mussel beds at deep-sea hydrothermal vents and cold seeps. Ecology Letters 6, 518-523.
1011 Veloso, M., Greinert, J., Mienert, J., De Batist, M., 2015. A new methodology for quantifying
1012 bubble flow rates in deep water using splitbeam echosounders: Examples from the Arctic
1013 offshore NWSvalbard. Limnology and Oceanography: Methods 13, 267-287.
1014 Vogt, P.R., Crane, K., Sundvor, E., Max, M.D., Pfirman, S.L., 1994. Methane-generated(?)
1015 pockmarks on young, thickly sedimented oceanic crust in the Arctic: Vestnesa ridge, Fram strait.
1016 Geology 22, 255-258.
1017 Weber, T.C., Mayer, L., Jerram, K., Beaudoin, J., Rzhanov, Y., Lovalvo, D., 2014. Acoustic
1018 estimates of methane gas flux from the seabed in a 6000 km^2 region in the Northern Gulf of
1019 Mexico. Geochemistry, Geophysics, Geosystems 15, 1911–1925, doi:10.1002/2014GC005271.
1020 Wenau, S., Spieß, V., Pape, T., Fekete, N., 2017. Controlling mechanisms of giant deep water
1021 pockmarks in the Lower Congo Basin. Marine and Petroleum Geology 83, 140-157.

1022 Westbrook, G.K., Thatcher, K.E., Rohling, E.J., Piotrowski, A.M., Pälike, H., Osborne, A.H.,
1023 Nisbet, E.G., Minshull, T.A., Lanoisellé, M., James, R.H., Hühnerbach, V., Green, D., Fisher,
1024 R.E., Crocker, A.J., Chabert, A., Bolton, C., Beszczynska-Möller, A., Berndt, C., Aquilina, A.,
1025 2009. Escape of methane gas from the seabed along the West Spitsbergen continental margin.
1026 Geophysical Research Letters 36, L15608, doi:10.1029/2009GL039191.
1027 Whiticar, M.J., 1999. Carbon and hydrogen isotope systematics of bacterial formation and
1028 oxidation of methane. Chemical Geology 161, 291-314.
1029 Whiticar, M.J., Werner, F., 1981. Pockmarks: Submarine vents of natural gas or freshwater
1030 seeps? Geo-Marine Letters 1, 193-199.
1031 Woolf, D.K., 1993. Bubbles and the air-sea transfer velocity of gases. Atmosphere-Ocean 31,
1032 517-540.
1033 Woolf, D.K., Thorpe, S., 1991. Bubbles and the air-sea exchange of gases in near-saturation
1034 conditions. Journal of Marine Research 49, 435-466.
1035
1036 **Captions**
1037 **Figures**
1038 **Figure 1**. a. Location map showing Vestnesa Ridge in the Fram Strait. b. Names of active
1039 pockmarks along the eastern crest of Vestnesa Ridge; c. regional multibeam bathymetric map
1040 showing sampling locations. Location of sediment cores used in this paper (see Table 1), ship
1041 track lines of the six bottom photography tows that collected over 5000 images, and the
1042 photomosaics TC1-3 are indicated. To be noted the location of marker CAGE888 and
1043 CAGE895.
1044 **Figure 2**. a. Bathymetry of Lomvi pockmark. The photomosaics TC1-3 and the subsurface
1045 seismic shown in e and f of this figure are indicated. b. Amplitude of Lomvi. The purple color
1046 show high amplitude most likely related to the presence of free gas within the sediment. **c.**

1047 Frequency decomposed image of the seafloor where areas that appear whitish color show good
1048 response in all three frequencies indicating free gas, gas hydrate or carbonates, whereas areas
1049 that show darker color have poor response in all frequencies. d. pink and light blues dots
1050 represent the centre of the hydroacustic footprints (radius of 73 m) of gas bubbles. **e.** Seismic
1051 profile showing the chimney structure; the white box is shown in **f** and outline high amplitude
1052 anomalies in the gas chimney beneath Lomvi that stack and align vertically, cutting across
1053 disrupted strata and terminating into the pits at the seafloor. White lines indicate migration
1054 pathways.
1055 **Figure 3**. a. Photomosaic TC1 from TC lowering CAGE-HH 892 and b. interpretation. White
1056 squares on photomosaic indicate the areas details on Fig. 4.
1057 **Figure 4**. a. Carbonate crust, ca 5-10 c thick. Sediment underneath the crust has been scoured. b.
1058 Large patch of white bacterial mat; throughout the image highlighted against the iron sulfide
1059 bearing black sediment. High density of Siboglinid tubeworms protrude ca 2-4 cm above the
1060 sediment surface. Two fish appear to feed on bacterial mats. c. Bacterial mats exhibit a network
1061 structure. Bushes of Siboglinid tubeworms protrude ca 2-4 cm above the sediment surface. d.
1062 Sparse small carbonate blocks associated with patches of bacteria. Several fish and benthic
1063 animal tracks are obvious in the image. e. Massive carbonate blocks with ca 2m of elevation
1064 provide a hard substrate for epifaunal invertebrates (e.g., erect bryozoans and spherical sponges)
1065 and structure for mobile fauna. Close-up showing abundant sponges *Cinachyra.* f. Soft sediment,
1066 mud bottom with dense bushes of Siboglinid tubeworms and bacterial mats.
1067 Green laser dots spaced 20 cm apart (these are present in all images and provide the ability to
1068 scale features in all images; when not present the scale is indicated).
1069 **Figure 5**. a) shows the depth of the TowCam (blue) and the seafloor (red line), and the timing of
1070 the photos, along a track on the flank of Lomvi pockmark as indicated in b). c) and d) show the
1071 sedimented seafloor at the edge of the pit, sloping towards its center. Bacterial mats associated

1072 with diffuse outflow are observed along these slopes of actively venting pits. The position of the
1073 photos in indicated in a). Apparent cropping of images corresponds to the TowCam frame
1074 blocking partially the field of view of the camera.
1075 **Figure 6**. a. Sparse angular ice-rafted clasts at the seafloor in the pockmark area. b. Crinoid at
1076 the seafloor in the pockmark area. Crinoids are passive suspension feeder, considered "current-
1077 lovers" and can be used as indicators of bottom water current. The mucus that covers the
1078 pinnules captures particles of food that floats by transported by bottom current. Green laser dots
1079 spaced 20 cm apart (these are present in all images and provide the ability to scale features in all
1080 images; when not present the scale is indicated).
1081 **Figure 7**. a. Gas hydrate in core catcher after sampling a core inside pockmark Lomvi. b. Gas
1082 hydrate pieces in the water column dislodged from seafloor during multicoring (Fig. 1). The
1083 pieces of gas hydrate were 5-8 cm in diameter. c. Thin pavement at the seafloor exposed by
1084 fissures in the indurated hydrate crust and thought to be sediment cemented by fine gas hydrate
1085 layers at CAGE895 marker.
1086 **Figure 8**. a. Relationship between stable carbon isotope composition ($\delta^{13}C$) of CH_4 and the
1087 molecular ratio C1/C2+3 in head space gas samples and gas hydrate samples (symbols shown as
1088 dashed outlines) plotted on a “Bernard’’ Diagram (after Bernard et al., 1978). The fields of
1089 microbial, thermogenic and mixed gases are defined after Whiticar (1999). All samples were
1090 collected from cores (Fig. 1c) in the same pockmark. Data from Smith et al., 2014 is an average
1091 from three gas hydrate samples collected from core GC929 (Fig. 1c). b. Gas source “Whiticar”
1092 diagram (Whiticar, 1999) with the sample measurements of the stable hydrogen (dD) and carbon
1093 (□13C) isotope compositions of CH4 in gas samples collect from both pockmarks in this study.
1094 **Figure 9**. Cartoon showing the main characteristics and processes occurring in Lomvi
1095 pockmarks. The seismic profile (from Fig.2c, f) shows the chimney underneath the pockmark. In
1096 the top half of the chimney enhanced reflections appear to cut across lithological boundaries and

are slightly inclined upwards towards the seafloor where terminate in the pits. The white lines indicate migration pathways. The enhanced reflection results from a strong impedance contrast due to the presence of free gas, gas hydrates and/or carbonates. The finding of fossil seep-related community and carbonate nodules (Ambrose et al., 2015) might explain some of those reflections. The pits are characterized by bacterial mats and scattered small blocks of carbonate and focused methane flares. The floor of the pockmark is characterized by Siboglinid tubeworms and bacterial mats. The diffused and focused fluid flows are indicated and the size of the fluxes are explained in the text, including relevant references. SMT=sulphate-methane transition zone. Orange arrows indicate diffused and focused fluid flow and orange number are from Table 3. The thermogenic production of methane occurs in deep sediment and feed the gas hydrates while biogenic methane production occurs in the entire sedimentary column.

Tables

Table 1. Data and samples collected during cruises from 2010 to 2015. Data already published and used here are indicated (Bünz et al., 2012; Smith et al. 2014, Plaza Faverola et al. 2015).

Table 2. Isotope and gas composition from head space gas and gas hydrate from gravity cores (GC) and multicores (MC) samples at different depth below the seafloor (cmbsf) collected in 2013 (CAGE13) and 2015 (CAGE15-2).

Table 3. Rate and fluxes from Lomvi and Lunde. The AOM rates reported in row *a* is from Hong et al. (2016) and T. Treude (unpublished data). The rates of methane carbon sequestrated as authigenic carbonate (row c) were calculated from the total carbonate precipitation rates and the fraction of dissolved inorganic carbon (DIC) produced by AOM reported by Hong et al. (2016). The output and consumption (rows *b, d, f*) were calculated from the corresponding flux and rate (rows *a, c, e*) and the area (Area in m^2) of each pockmark reported in this table. The calculations of water column methane flux and methane output are detailed described in the

Supplementary data.

Table 4. Compilation of pockmark location around the world with mechanism and time of formation, and fluid indicators at the seafloor.

Supplementary data

1. Methods

1.1 Free gas quantification

We analyzed data from the four surveys (Table 1, main text) using the Fledermaus Midwater software for a first evaluation of acquired files, and for the identification of bubble streams (flares). The number of files included in the survey, files containing flares, the number of flares and clusters (see 1.9 section for explanation about clustering) within the focus area (Lomvi and Lunde pockmarks) during each survey are given in Table 1SD.

1.2 Flow rate calculations

Accurate flow rate calculations from echosounder signal strength, or target strength (TS), can be performed if the rise velocity, bubble rising speed BRS (U(r) in equation 1), the bubble-size distribution BSD (N(r) in equation 1), and the backscatter cross sections, σ_{bs} of bubbles are known. The volumetric flow rate (Q) is given in e.g. Veloso et al. (2015);

$$Q = K \cdot 10^{\frac{TS}{10}} \quad (1)$$

$$K = \frac{\frac{4\pi}{3}\int_{r_1}^{r_2} N(r)U(r)r^3 dr}{\int_{r_1}^{r_2} N(r)\sigma_{bs}(r)dr}$$

However, the BSD and BRS are unconstrained since we do not have visual bubble observations. To estimate a range of flow rates we simplify the calculation by applying single rising speeds and single size bubble population, and then use end-member values for each parameters (see below). The flow rate calculation is then:

$$Q = 10^{\frac{TS}{10}} \frac{4\pi\ r^3 \cdot U}{3\ \Delta z \cdot \sigma_{bs}} \quad (2)$$

where Δz is the vertical bin size of the echosounder data. For each cluster, a representative TS value is obtained from observations and minimum/maximum flow rates are calculated from end-members of bubble sizes and rising speeds. We use 3 and 8 mm as minimum and maximum bubble size values respectively, with minimum and maximum rising speeds of 15 and 30 cm/s. In the following, we give details on the method, and discuss inherent uncertainties and report plausible flow rate ranges for the two pockmarks using data from 2012 (Table 2SD; Table 3).

1.3 Targets strength values

Beam compensated targets strength (TS) was calculated from the power of the returned acoustic signal, recorded by the echosounder. We used FlareHunter software developed in Veloso et al., (2015) for this calculation and for editing flares (removing backscatter from fish, seafloor, interference etc.) in order to find the representative target strength (TS) for each flare. Subsequently, as the bubble sizes and rising speeds are unknown, we used what we consider end-members of sizes and speeds in order to calculate the minimum and maximum flow rates of these flares. We calculated flow rates from the best insonification (highest TS values) in a layer 5-10 meters above the seafloor. Figure 1SD shows an example of the layer selected, the data

selected for analysis and some unwanted interference and seafloor scatter (yellow and red pixels). By avoiding the seafloor and interference from other acoustic instruments, we ensure that we do not overestimate subsequent flow rate calculations. The selected data was visualized in 3D (not shown here), using the split beam capability of the EK60 echosounder and further checked for interference (details in Veloso et al., 2015).

As the water column itself has some backscatter, very low amplitudes (in this case lower than -55 dB) were excluded and a geometric mean of the remaining target strength (TS) was calculated.

TS is related to a total backscatter cross section (σ_{bs}) by $TS = 10\log_{10}(\sigma_{bs})$ and this backscatter cross section comprises the sum of the acoustic scatter from a number of bubbles with different sizes. Bubbles of different sizes return different acoustic signals, depending on echosounder frequency, resonance frequency and damping effects (Medwin and Clay, 1997);

$\sigma_{bs}(r) = \frac{r^2}{\left[\left(\left(\frac{f_{R(r)}}{f}\right)^2 - 1\right)^2 + \delta^2\right]}$, where r is the bubble radius, f_R is the resonance frequency of the bubble, f is the echosounder frequency and δ is a combined damping coefficient comprised of re-radiation, viscous and thermal damping. Details are available in Veloso et al. (2015) and Medwin and Clay (1997). The damping coefficient δ is here a major unknown because the acoustic effect of hydrate coating on the bubble surface is largely unknown. Muyakshin and Sauter (2010), suggest that the K coefficient in equation 1 may vary by a factor of four if a hydrate film of 8µm is present compared to no hydrate formation.

1.4 Bubble rising speed (BRS)

Extensive work has been done in order to establish a relationship between bubble sizes and rising speeds and models have been suggested for bubbles both with and without surfactant (e.g. Leifer and Patro, 2002; Leifer et al., 2000; Mendelson, 1967; Woolf, 1993; Woolf and Thorpe, 1991). However, since we do not have visual bubble observations, we simply report 15 and 30 cm/s as

1182 the end members of bubble velocities regardless of their radius, which are consistent with
1183 reported speeds in the studies mentioned above. Generally, large bubbles with surfactant rise
1184 faster than bubbles without, so we can assume that bubbles coated with a thin hydrate film rise
1185 faster than bubbles of the same radius without hydrate coating. Therefore, if the bubbles are
1186 hydrate coated, the bubble rising speed and subsequently the flow rate is underestimated by our
1187 calculations, that assume no hydrate coating. The relative error induced by the choice of bubble
1188 rising speed models is ~16% (Veloso et al., 2015).

1189 **1.5 Bubble sizes**

1190 Veloso et al., (2015) used a Gaussian-like bubble size distribution peaking at 3mm, which was
1191 observed at the continental shelf and shelf-break west of Svalbard in 2012, and is consistent with
1192 observations at the Pascagoula Dome in the Gulf of Mexico (Weber et al., 2014). Sahling et al.
1193 (2009) used a peak radius of 5 mm, acquired from a survey of a mud volcano in the Black Sea. It
1194 is thus likely that the calculated flow rates based on a 3 mm bubble are underestimates and the 8
1195 mm overestimates, and detailed in situ observations at different flares along the Vestnesa Ridge
1196 are required instead.

1197 **1.6 Bubble ellipticity**

1198 We assume that bubbles are spherical, which is probably true for small bubbles, but observations
1199 have shown that larger bubbles tend to be oblate (e.g. Leifer and Patro, 2002). The volume of an
1200 ellipsoid bubble with a 3 mm horizontal axis, which is detected by the echosounder, and 2 mm
1201 vertical axis, may be overestimated by up to 50%, if they are assumed spherical. Bubbles may be
1202 tilted as they rise through the water, which implies that, for a bubble with axes 3 and 2mm long,
1203 the upper limit of this overestimation is 50%.

1.7 Calculations based on water column data 5 – 10 meters above the seafloor

Some gas may be dissolved below the layer (5 – 10 meters above the seafloor) selected for the calculations. Single bubble models (McGinnis et al., 2006) predict that roughly 10% of the seafloor emission may be dissolved in the first five meters, assuming there is no hydrate rim inhibiting the dissolution. This may imply an underestimation of max 10% for the here calculated flow rates.

1.8 Summary of uncertainties

Large uncertainties arise from unknown physical bubble properties (e.g. bubble rising speeds, bubble sizes, hydrate rims, bubble shapes). We believe that the calculated flow rates, once all uncertainties are considered, underestimate the real flow rates, and that the real flow rates may be up to five times higher than the calculated values.

In all of our calculations, we used the same range of bubble sizes and rising speeds and assumed spherical bubbles without hydrate rim. The temperature and salinity near the seafloor varies insignificantly (T = -0.8°C, S=35 PSU), and so the physical conditions in the water column may not cause variations in flow rates. However, we ignore if bubble sizes are constant or vary between the surveys or between flares.

The flow rates calculated from the TS data show similar ranges (typically 3 - 100 ml min^{-1}) during 2010, 2012 and 2013. However, in 2015 we found higher flow rates overall and significantly higher rates at one location, based on three observations. A detailed analysis of these parameters, uncertainties, calculated fluxes, and temporal and spatial variations, will be the focus of a follow-up paper, and are out of the scope of this paper.

1.9 Flare clustering

We consider the echosounder coverage at the seafloor to identify where flare observations overlap geographically, and calculate TS values and flow rates representative for each group of flares (clusters). Applying clustering allows us to estimate the total free gas flow in a specific

1229 area, providing that we have 100% echosounder beam coverage, which is the case for all our
1230 surveys of Lomvi and Lunde. The resulting flow rates for Lomvi and Lunde 2012 are given in
1231 Table 2SD. Conversion from in situ flow rates (Table 2SD) to flux values (Table 3) were made
1232 considering the pit diameter of 50 meters and the ideal gas law.
1233
1234 **Captions:**
1235 Figure 1SD. Photomosaics for areas 1 (a), 2 (b), and 3 (c) in Figure 2. Photomosaics have been
1236 constructed from TowCam images after distorsion and illumination correction, renavigation of
1237 the deep-towed vehicle, and blending to remove seams among images (see text for details and
1238 references). All photomosaics are shown at the same scale, and the best estimate of the limits in
1239 UTM X and Y are given for each of them.
1240 **Figure 2SD**. Zoom-in on two flares near the seafloor. The 5 m meters deep layer for evaluation
1241 is highlighted and the backscatter from the bottom and interference from other acoustic
1242 instruments (red and orange pixels) is easily recognizable. The Graphical User Interface
1243 'FlareHunter' (Veloso et al., 2015) was used to visualize, analyze and process hydroacoustic data
1244 showing bubble release in echograms.

1245 **Table 1SD**. Water column hydroacoustic data used for flare detection. The column headers are
1246 self-explanatory. The focus area covers the Lomvi and Lunde pockmarks.
1247 **Table 2SD**. Water column hydroacoustic data and modeled flow rates. The cluster positions
1248 (bold) are calculated means of the UTM32N positions of the associated flares. The column TS
1249 contains the observed value from each observation and the calculated geometric mean of these
1250 are shown in bold. The modeled flow rates for each cluster are based on the cluster TS (bold) and
1251 the bubble size (r) and rising velocity (U) used in the model. The Beam radii represent the
1252 footprint size (radius) of the echosounder at the seafloor.

Table 3SD. Parameters used for total flow rate and total output calculation for Lomvi and Lunde. The cluster of flow rates (ml min-1; raw *d*) is calculated considering that the free gas emanating from an area corresponding to one pit of 25m radius. The number of clusters made of flares found within each of the two pockmarks during the 2012 survey is indicated in row *f*. Row *g* is the sum of the flow rates for each of the pockmarks and row *h* shows the total output of free gas to the water column for each pockmark. The conversion from flow rates to flux values was obtained using the ideal gas law.

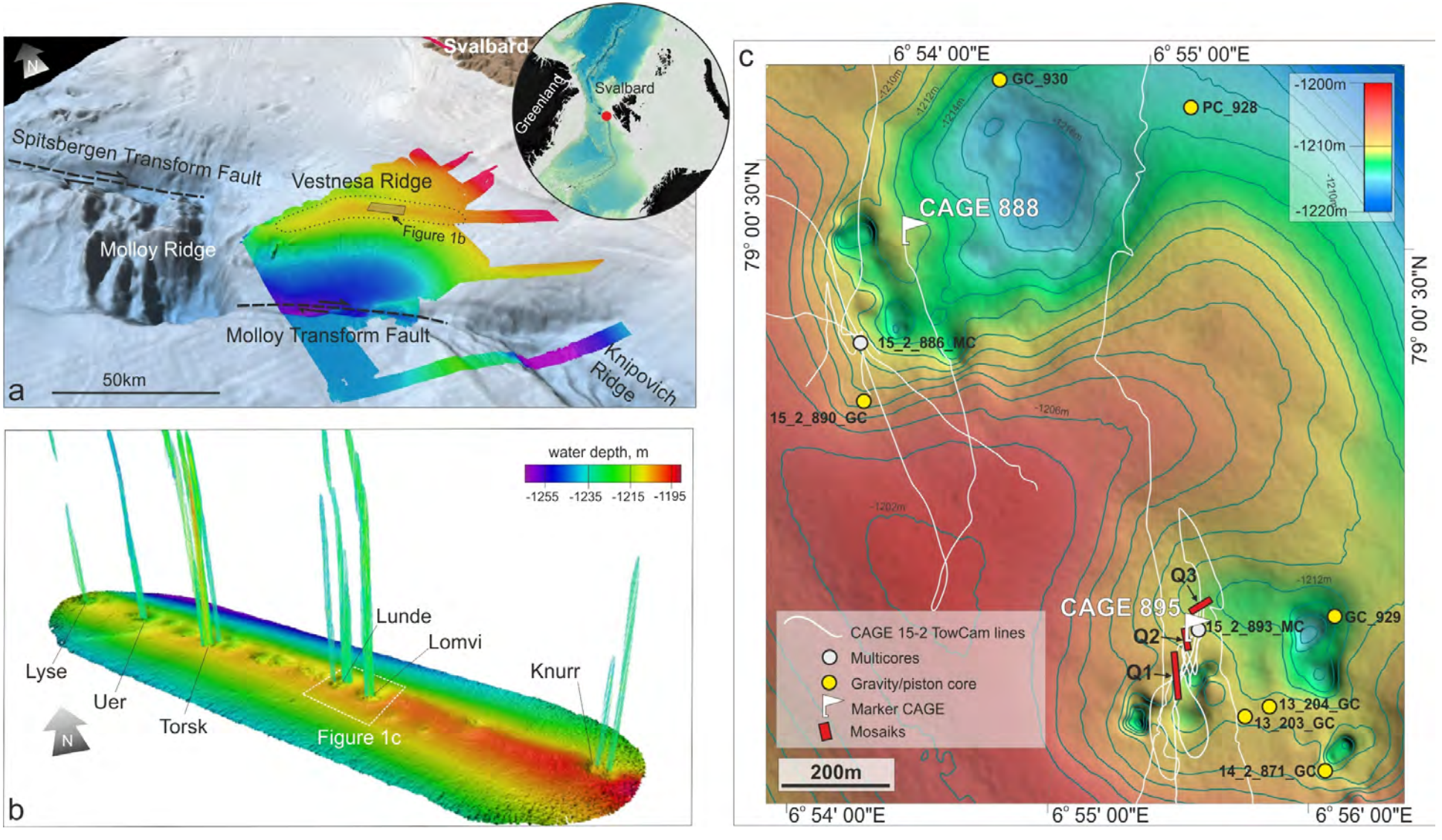
a
N
Svalbard
Greenland
Svalbard
Spitsbergen Transform Fault
Vestnesa Ridge
Figure 1b
Molloy Ridge
Molloy Transform Fault
Knipovich Ridge
50km
b
water depth, m
-1255 -1235 -1215 -1195
Lyse
Uer
Torsk
Lunde
Lomvi
Knurr
Figure 1c
N
c
6° 54' 00"E
6° 55' 00"E
6° 56' 00"E
79° 00' 30"N
GC_930
PC_928
-1200m
-1210m
-1220m
CAGE 888
15_2_886_MC
15_2_890_GC
-1206m
-1202m
-1212m
CAGE 895
Q3
Q2
Q1
15_2_893_MC
GC_929
13_204_GC
13_203_GC
14_2_871_GC
CAGE 15-2 TowCam lines
Multicores
Gravity/piston core
Marker CAGE
Mosaiks
200m

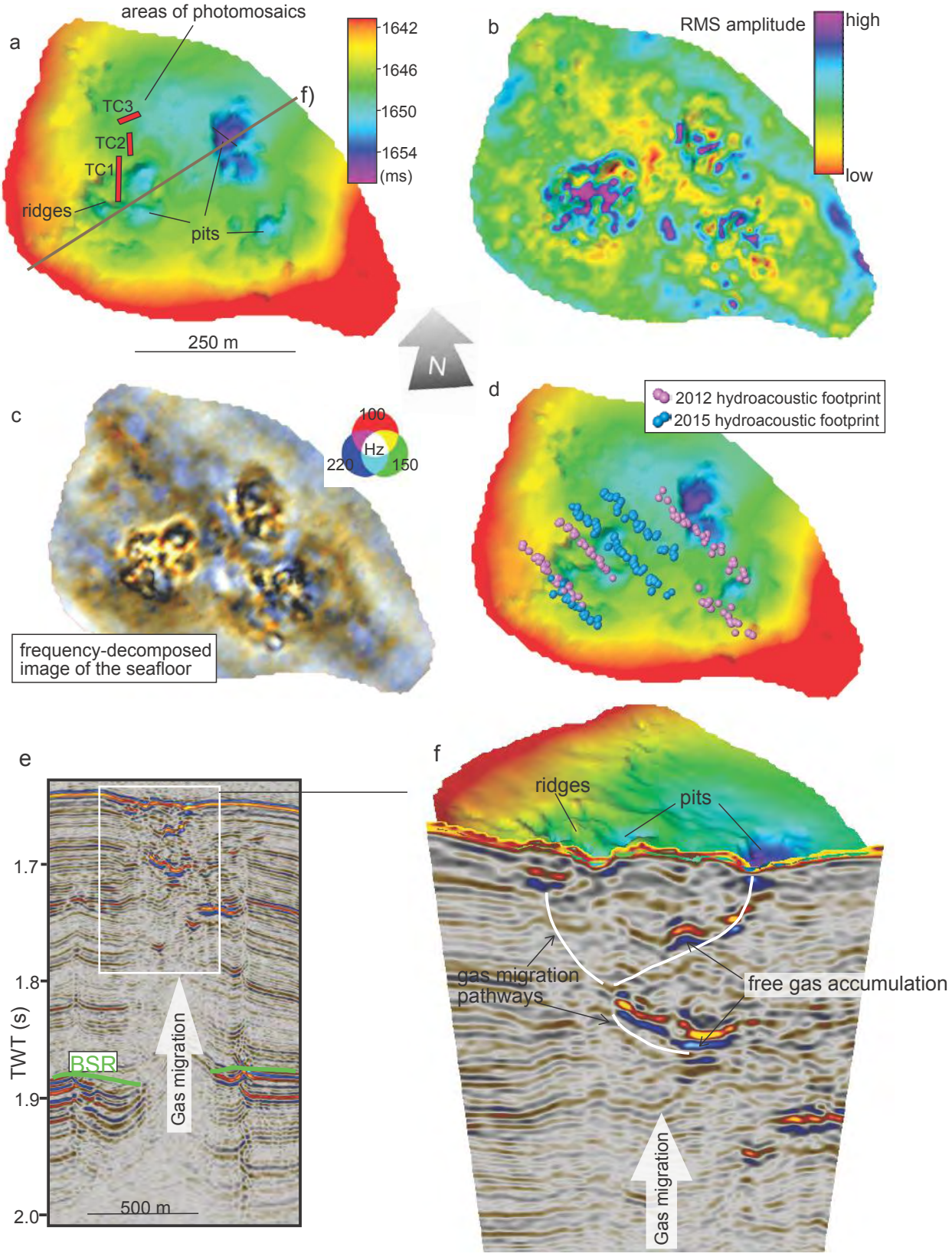
a
areas of photomosaics
TC3
TC2
TC1
f)
ridges
pits
1642
1646
1650
1654
(ms)
250 m
N
b
RMS amplitude
high
low
c
100
Hz
220
150
frequency-decomposed
image of the seafloor
d
2012 hydroacoustic footprint
2015 hydroacoustic footprint
e
1.7
1.8
1.9
2.0
TWT (s)
BSR
Gas migration
500 m
f
ridges
pits
gas migration
pathways
free gas accumulation
Gas migration


Photomosaic
TC1
Carbonate slab and blocks
Bacterial mats
Seep tubeworms (isolated and bushes)
Angular ice-rafter clasts
5m
a
b
N

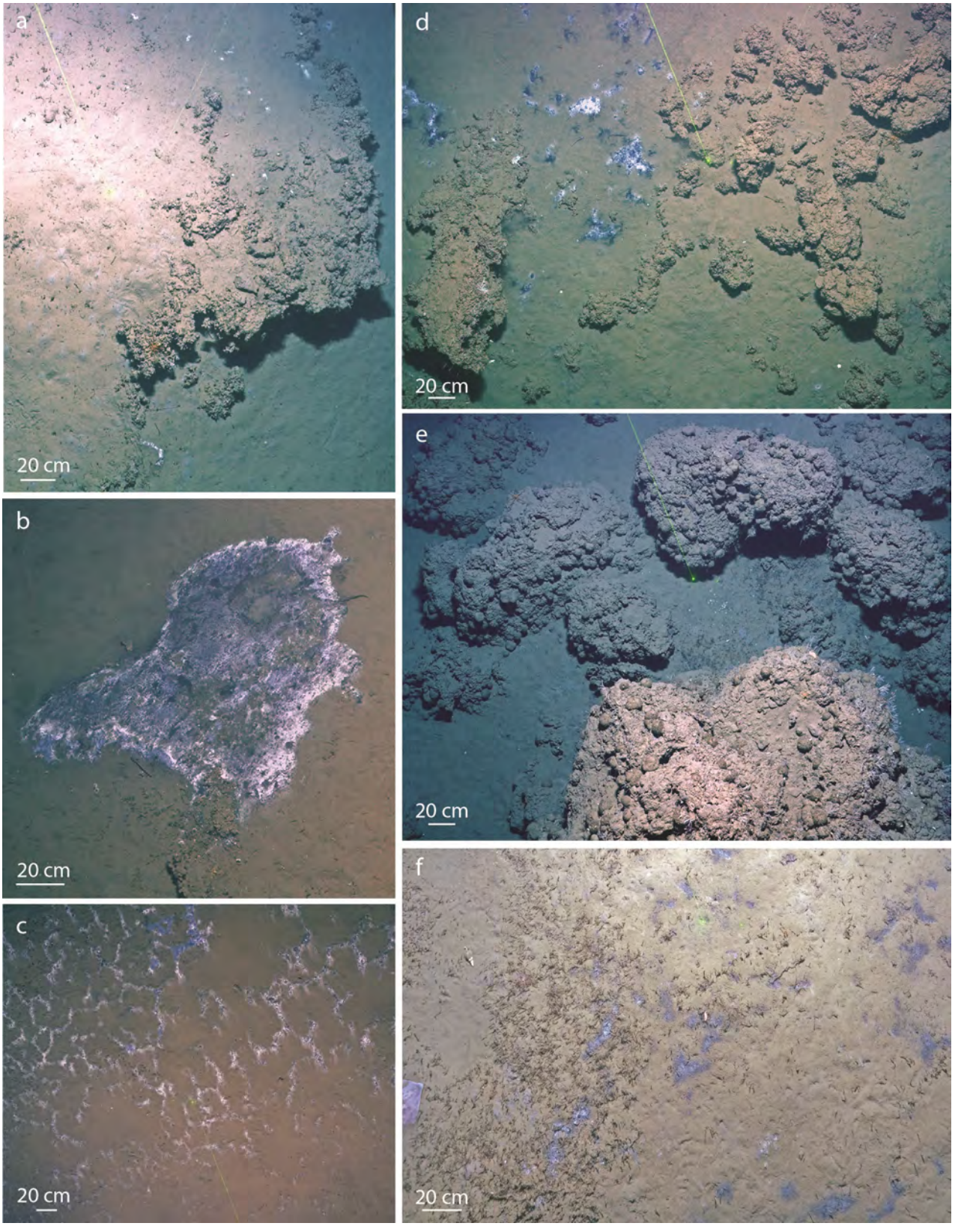
a
20 cm
b
20 cm
c
20 cm
d
20 cm
e
20 cm
f
20 cm

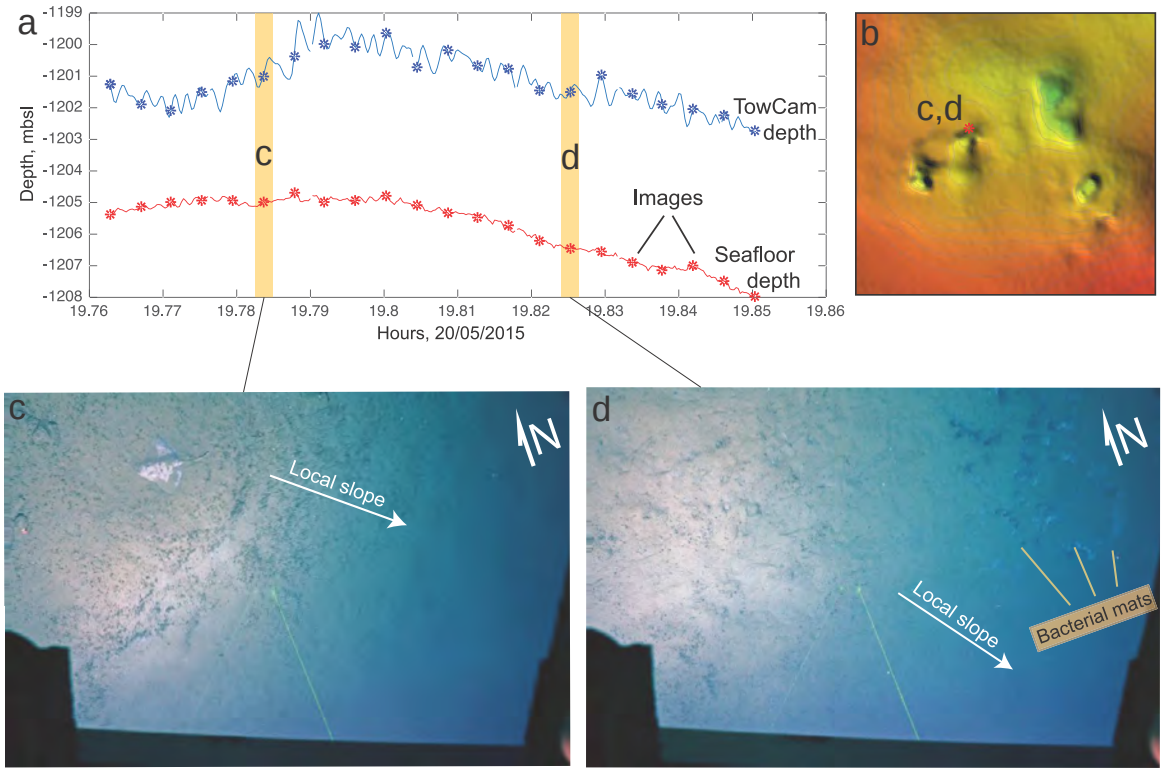
a
b
c
d
c,d
TowCam
depth
Images
Seafloor
depth
Depth, mbsl
Hours, 20/05/2015
-1199
-1200
-1201
-1202
-1203
-1204
-1205
-1206
-1207
-1208
19.76
19.77
19.78
19.79
19.8
19.81
19.82
19.83
19.84
19.85
19.86

c
N
Local slope

d
N
Local slope
Bacterial mats

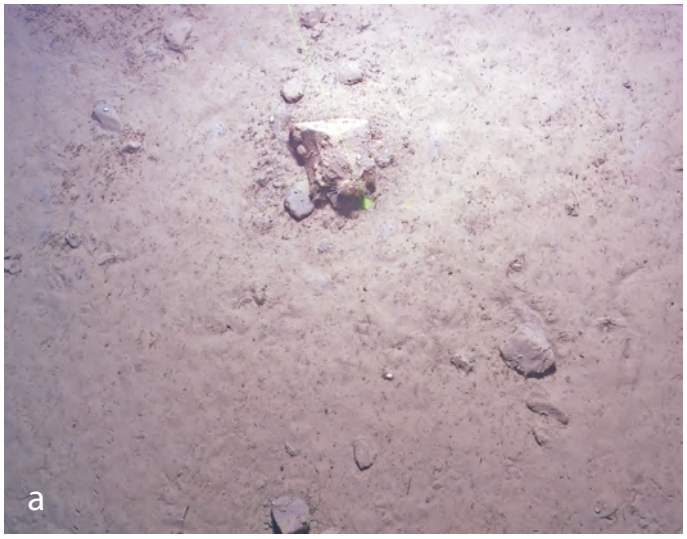
a


b


a

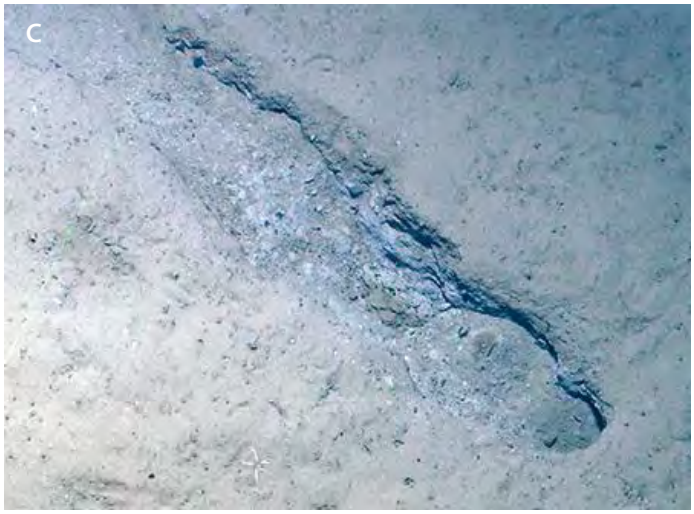
c


b

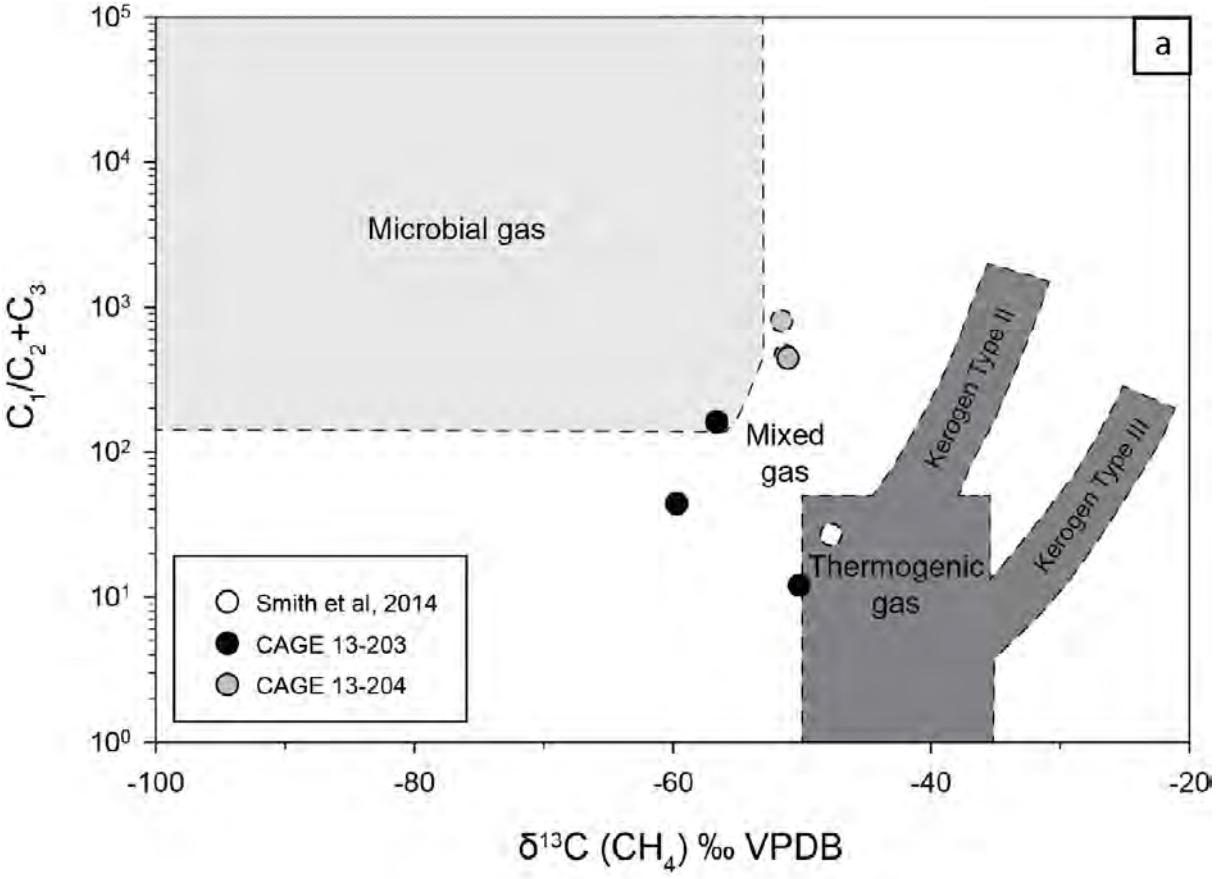
a
Microbial gas
Mixed gas
Thermogenic gas
Kerogen Type II
Kerogen Type III
Smith et al, 2014
CAGE 13-203
CAGE 13-204
C_1/C_2+C_3
$\delta^{13}C$ (CH_4) ‰ VPDB

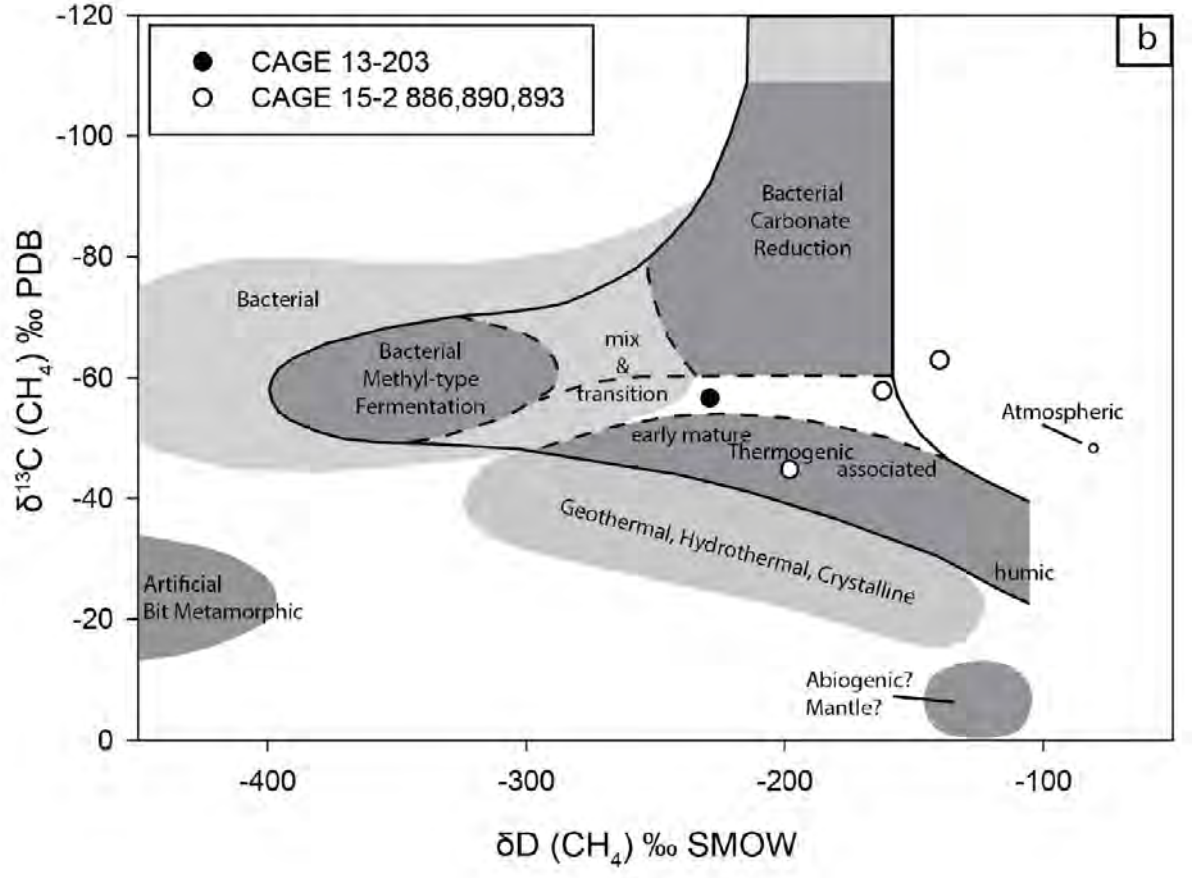
b
CAGE 13-203
CAGE 15-2 886,890,893
Bacterial Carbonate Reduction
Bacterial
Bacterial Methyl-type Fermentation
mix & transition
early mature
Thermogenic associated
Atmospheric
Geothermal, Hydrothermal, Crystalline
humic
Artificial Bit Metamorphic
Abiogenic? Mantle?
$\delta^{13}C$ (CH_4) ‰ PDB
δD (CH_4) ‰ SMOW

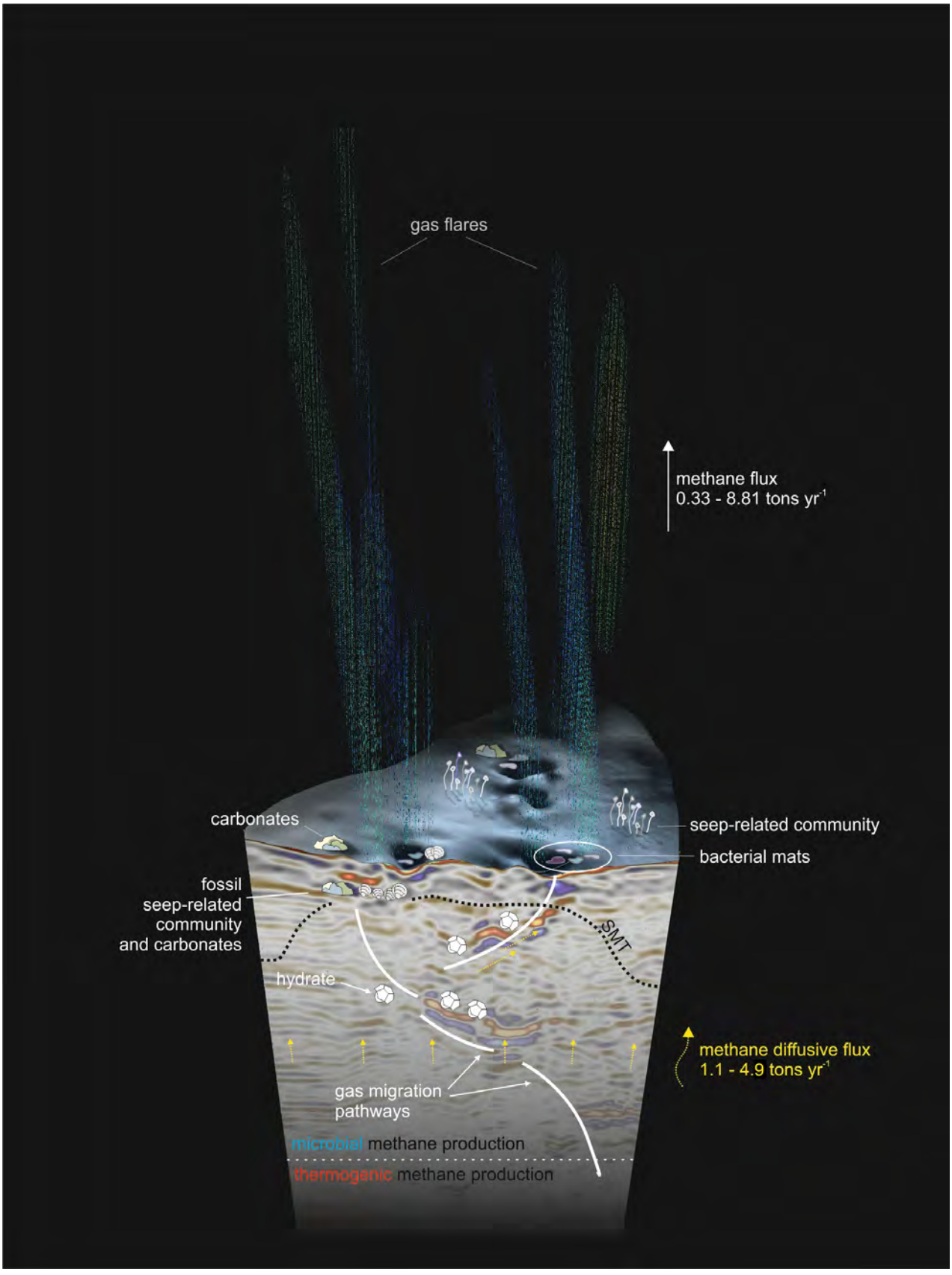
gas flares
methane flux
0.33 - 8.81 tons yr-1
carbonates
seep-related community
bacterial mats
fossil
seep-related
community
and carbonates
SMT
hydrate
methane diffusive flux
1.1 - 4.9 tons yr-1
gas migration
pathways
microbial methane production
thermogenic methane production

a.

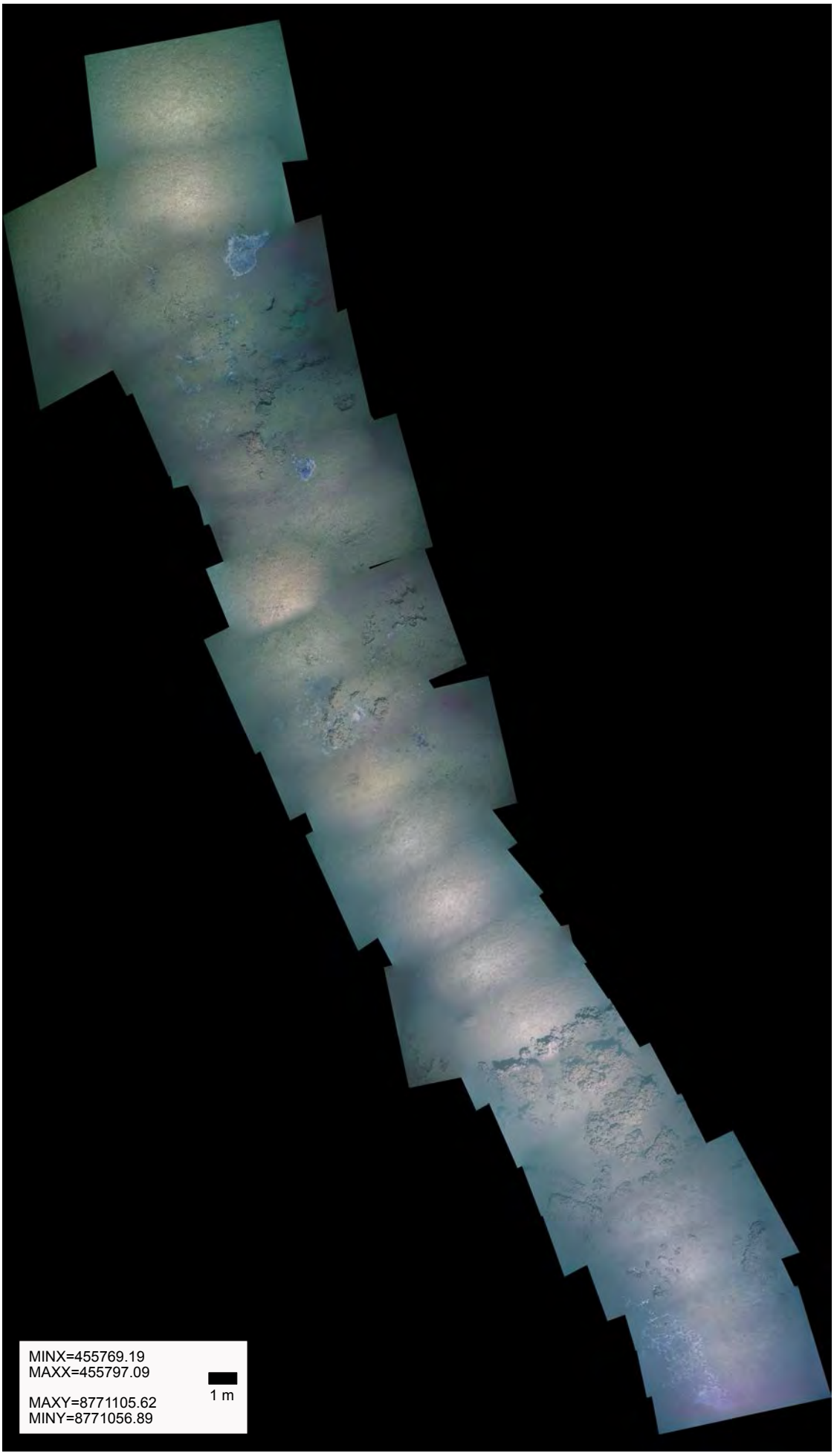

TOWCAM MOSAIC 1

b.

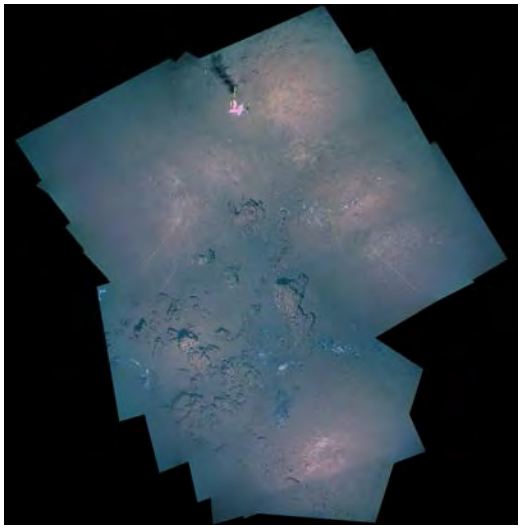

MAXX=455802.22
MINX=455815.77

MAXY=8771127.86
MINY=8771114.13

1 m

TOWCAM MOSAIC 2

c.

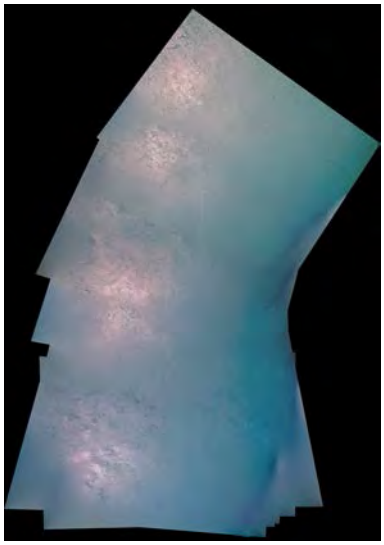

MAXX=455828.96
MINX=455819.04

MAXY=8771153.06
MINY=8771138.94

1 m

TOWCAM MOSAIC 3

Data used in this paper	CRUISE (year collected; R/V)	References
Geophysics		
Multibeam bathymetry	CAGE13 (2013; Helmer Hanssen)	Plaza Faverola et al. (2015)
3D seismic data	CAGE13 (2013; Helmer Hanssen)	Plaza Faverola et al. (2015)
Seafloor observations (TowCam)	CAGE15-2	This study
Seafloor-subseafloor correlations		This study
Water column hydroacoustics (flare detection) using single-beam echo sounder	2010 (Jan Mayen)	Bünz et al. (2012)
	2012 (Helmer Hanssen)	Smith et al. (2014)
	CAGE13 (2013; Helmer Hanssen)	Mienert, unpublished data
	CAGE 15-4 (2015; Helmer Hanssen)	Bünz, unpublished data
Gas measurements		
Head space gas	CAGE15-2 (2015; Helmer Hanssen)	This study
	CAGE13 (2013; Helmer Hanssen)	Mienert, unpublished data
Gas hydrate	CAGE15-2 (2015; Helmer Hanssen)	This study
	2012 (R/V Helmer Hanssen)	Smith et al. (2014)
Fossil seep-related community and carbonate nodules	CAGE13 (2013; Helmer Hanssen)	Ambrose et al. (2015)
AOM rate (model estimate)	JR211(2008; James Clark Ross); CAGE13 (2013; Helmer Hanssen)	Hong et al. (2016)
AOM rate (direct measurements)	RV Poseidon 419 expedition (2011; Poseidon)	T. Treude, unpublished data
Total AOM consumption		This study
Methane sequestration rate through authigenic carbonates		This study
Total consumption of methane-C through carbonate precipitation		This study
Water column methane flux		This study
Water column methane output		This study

Core Site	Depth (cmbsf)	Sample Type	δ13C-CH4 ‰ VPDB	δD-CH4 ‰ VSMOW	C1/C2+C3
HH13-203GC	75	head space gas^	-50.2	-	12
HH13-203GC	130	head space gas^	-59.7	-	44
HH13-203GC	175	head space gas^	-56.6	-229	161
HH13-204GC	214	head space gas*	-51.1	-	443
HH13-204GC	594	gas hydrate*	-51.3	-	463
HH13-204GC	594	gas hydrate*	-51.6	-	801
15-2-886MC	29-32	head space gas#	-62.9	-140	-
15-2-893MC	13-15	head space gas#	-57.8	-162	-
15-2-890GC	300	head space gas#	-44.8	-198	-

easured at Hydroisotop GmbH - Schweitenkirchen, Germany

Research-UFZ, gas compostions at GEOMAR Helmholtz Centre for Ocean Research Kiel

l at Isolab B.V., Neerijnen The Netherlands

	Diffuse fluid regime (modeled results)		**Focused fluid regime 1 pit** (diameter 50 m)		**Bubbling site**
	Lomvi	Lunde	Modeled results	Direct measurements**	*(10% of the pit area)*
Area (m2)	628.000	7,536,000	ca 1,960	ca 1,960	196
a. AOM rate (mmol m-2 day-1)	0.3-1.1	0.3-1.1	44	1-10	NA
b. Total AOM consumption (tons yr-1)*	1.1-4.1	1.3-4.9	0.5	0.05-0.5	NA
c. Methane sequestration rate through authigenic carbonates (mmol m-2 d-1)	0.1-0.3	0.1-0.3	35	NA	NA
d. Total consumption of methane-C through carbonate precipitation (tons yr-1)*	0.3-1.0	0.3-1.2	0.4	NA	NA
e. Water column methane flux (mmol m-2 d-1)	Very small	Very small	Small	NA	13-390
f. Water column methane output (tons yr-1)	Very small	Very small	0.33-8.81	NA	0.03-0.88

* Hong et al. (2016)
**T. Treude (unpublished data)
NA: not available

Pockmark location	Water depth	Mechanisms of formation	Formation time	Fauna	Carbonate	Gas Hydrate	References
Arctic Ocean (Vestnesa Ridge)	1200 m	faults and fractures that act as a pathway for fluid migration	since 2.7 Ma ago	chemosynthetic communities	carbonates of various shapes	gas hydrates at different depth bsf	Vogt et al., 1994; Bünz et al., 2012; Plaza-Faverola et al., 2015; this
Arctic Ocean (Spitsbergen	110-130 m	tectonic controls (orientation of				above GHSZ	Forwick et al., 2009
Barents Sea	200 - 1270 m	gas pressure and faults		chemosynthetic communities		gas hydrates at different depth s bsf	Solheim and Elverhoi 1985, 1993; Chand et al.,
SW Barents Sea (Loppa High)	350 m	climate change-induced destabilisation of methane hydrates	since 15 cal kyr BP			no hydrates recovered	Pau et al., 2014
Bering Sea (Alaska)	<200 m	gas migration through faults and				above GHSZ	Abrams, 1992
Norwegian Sea (Giant Trol)	300 m	gas hydrate dissociation	since last deglaciatio		carbonate blocks	no hydrates recovered	Mazzini et al., 2017
Norweian Sea ("Unit-pockmarks")	300-700 m	reservoired gas acts as a dynamic pump			carbonate blocks	no hydrates recovered	Hovland et al., 2010
Norwegian Sea (Nyegga region)	700 m	vigorous gas venting system trhough chymney and faults		chemosynthetic communities	carbonates of various shapes	massive gas hydrates at different depth s bsf	Plaza-Faverola et al., 2010
NE Atlantic margin	400-1500m	hydrate stability changes				massive gas hydrates at different depths bsf	Mienert et al., 1998

Pockmark location	Water depth	Mechanisms of formation	Formation time	Fauna	Carbonate	Gas Hydrate	References
strait between Norway and Denmark (Skagerrak)	100-200 m	diapirically deformed plastic clay		chemosynthetic communities		above GHSZ	Hovland 1991
Canada (Pacific margin)	130-250 m	formation inside iceberg ploughmarks		unusual high abundance of non-chemosynthetic fauna	carbonate chimneys	above GHSZ	Halliday et al., 2008; Barrie et al., 2011
North Sea, UK sector (Witch Ground Basin)	100-150 m	degradation of subseabed permafrost ice				above GHSZ	Long, 1992
Atlantic Ocean (Belfast Bay,	30	escape of biogenic natural gas				above GHSZ	Kelley et al., 1994
Pacific Ocean (Big Sur, California)	900^1200 m		since 45 000 yr BP			no hydrates recovered	Paull et al., 2002
Gulf of Mexico	100-500 m	fault systems linked to active salt deformation and faulting		chemosynthetic communities	carbonate buildups	hydrate mounds and massive accumulation of gas hydrate in pockmarks below the upper edge of GHSZ	Sassen et al., 2001, 2003
Atlantic Ocean (Santos Basin, Brazilian continental slope)	400 - 900 m	salt diapirism		chemosynthetic communities , deepwater coral mounds		no hydrates recovered	Sumida et al., 2004; de Mahiques et al., 2017
SW Africa (Niger delta)	1100-1250 m	gas hydrate dissolution				massive gas hydrates at different depths bsf	Sultan et al., 2010

Pockmark location	Water depth	Mechanisms of formation	Formation time	Fauna	Carbonate	Gas Hydrate	References
SW Africa (giant Regab pockmark, Congo deep-sea channel)	3160 m	self-sealing processes and lateral spreading of rising fluids through fractures		mussel, tubeworm and clams	massive carbonate crusts that form thick elevations	at the seafloor	Marcon et al., 2014
SW Africa (Hydrate Hole, Black Hole, and Worm Hole in Northern Congo Fan)	3100 m	salt-tectonic faulting	several hundred thousand years	vesicomyid clams, tubeworms (Siboglinidae) and non-chemosynthetic organisms shrimp)	carbonates of various shapes	below 50 cm	Sahling et al., 2007; Wenau et al., 2017
South China Sea (N Zhongjiannan Basin)	600-1400 m	listric faults providing fluid				no gas hydrate recovered	Chen et al., 2015
South China Sea (mega-pockmarks near the Xisha Uplift)	700	faults providing fluid pathways				no gas hydrate recovered	Sun et al., 2011
E Atlantic (Gulf of Cadiz)	300 - 400 m	expulsion of biogenic gas and also to thermogenic gas coming from the volcanic/diapir		chemosynthetic fauna	autigenic carbonates	gas hydrates in the sediment column	Casas et al., 2003
central Mediterranean Sea (Zannone Giant Pockmark)	110 - 130 m	normal faults acting as main conduits	since 6 ky BP	bacterial mats	lithified pavements	above GHSZ	Ingrassia et al., 2015

Pockmark location	Water depth	Mechanisms of formation	Formation time	Fauna	Carbonate	Gas Hydrate	References
W Mediterranean Sea (TASYO field, Gulf of Cadiz)	500 - 2000 m	episodic dissociation of gas-hydrate-rich sediment tectonic and		bacterial mats, bivalve mounds of Calyptogena sp., tubeworm Pogonophora sp.	carbonate crusts	above GHSZ	Somoza et al., 2003
SW Mediterranean Sea (Gulf of Cadiz)	200 - 400 m	efflux of gas through the seafloor sediments				above GHSZ	Baraza and Ercilla, 1996
E Mediterranean Sea (Patras Gulf, Greece)	20 - 80 m	gas expulsion triggered by earthquake				above GHSZ	Hasiotis et al., 1996
E Mediterranean Sea (Patras and Corinth gulfs, Greece)	20-40 m	gas venting and groundwater seepage		rich fauna		above GHSZ	Christodoulou et al., 2003
E Mediterranean Sea (Iskenderun Bay, SE Turkey)	70 m	Sub-surface fault zones as conduits for gas migration, hydraulically active during or shortly after earthquakes.	protracted seepage of gas-charged fluids		buried carbonate	above GHSZ	Garcia-Garcia et al., 2004
NW Black Sea (Dnepr paleo-delta)	90 m	fluid/gas pathways relocated by carbonate formation		bacterial mat surrounded by Tunicates	carbonate-cemented sediment	above GHSZ	Naudts et al., 2008
E Black Sea	100-2000 m	local subsidence and faulting due to the escape of gas				hydrates at different depths bsf	Ergün et al., 2002

Pockmark location	Water depth	Mechanisms of formation	Formation time	Fauna	Carbonate	Gas Hydrate	References
Western Indian margin	20-260 m	deep-seated faults, fluid seeps dewatered the sediment and caused collapse structures, dissociation (?) of gas hydrates				in pockmarks below upper edge of GHSZ	Karisiddaiah and Veerayya, 2002
NW Shelf of Australia (Yampi Shelf and Timor Sea region)	50-100 m	Hydrocarbon migration-seepage pathways appear to be controlled by the reactivation of pre-existing fractures and dykes within the basement		more diverse biota than in non seep-sites	crusts of cemented bioclastic material	above GHSZ	Rollet e al., 2006

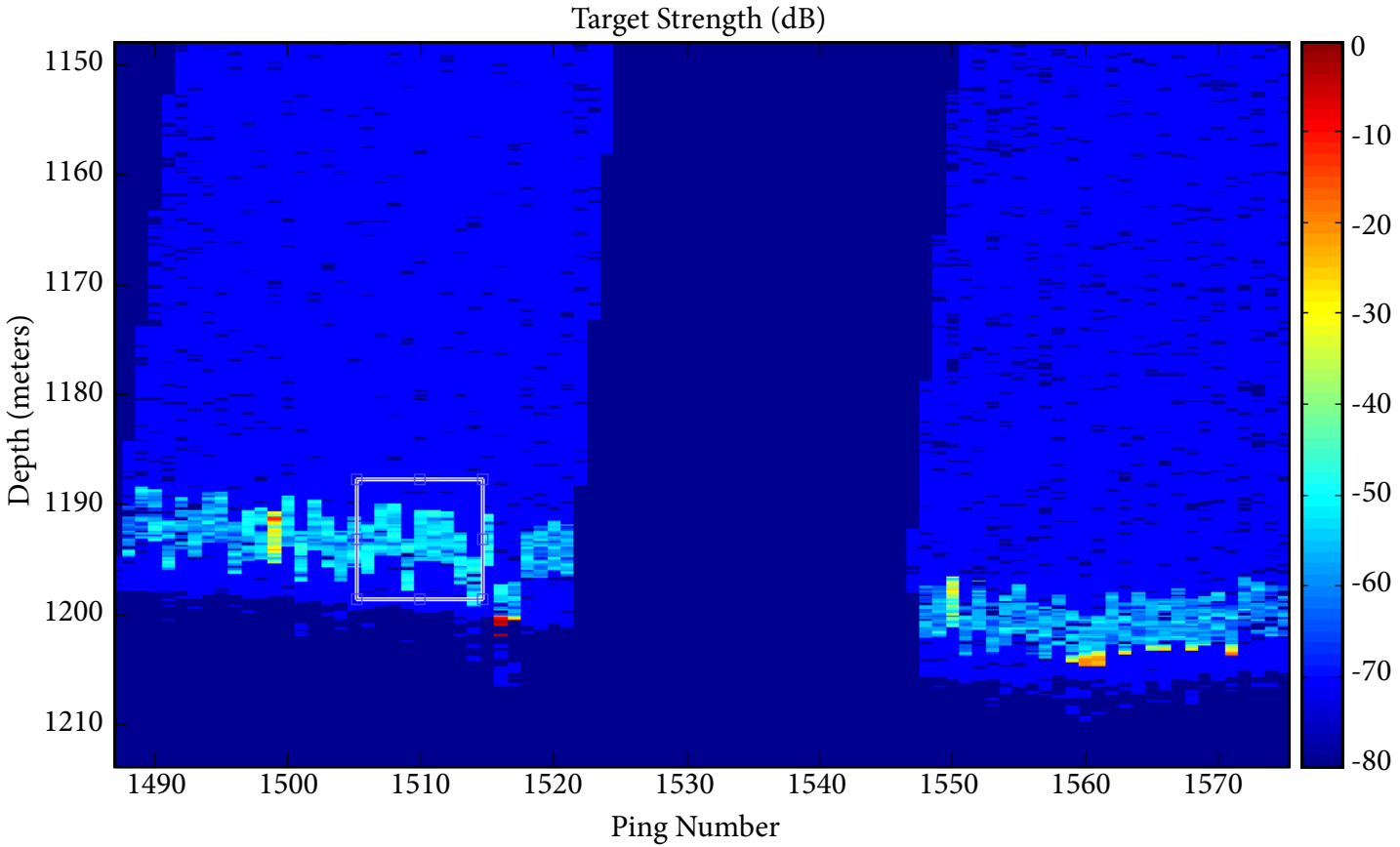
Target Strength (dB)
Depth (meters)
1150
1160
1170
1180
1190
1200
1210
1490
1500
1510
1520
1530
1540
1550
1560
1570
Ping Number
0
-10
-20
-30
-40
-50
-60
-70
-80

CRUISE (year collected; R/V)	# flare observations in Lomvi and Lunde	# flare clusters in Lomvi and Lunde
2010 (Jan Mayen)	11	3
2012 (Helmer Hanssen)	9	5
CAGE13 (2013; Helmer Hanssen)	23	4
CAGE 15-4 (2015; Helmer Hanssen)	13	6

Cluster / Pockmark	Hydroacoustic data: UTM 32N Coordinates East	North	Depth (m)	Beam radii	TS (dB)	Modelled flo r=3mm U=15cm/s
					2010	
cluster 1	**455317.9152**	**8771635.009**			**-52.238**	**4.210**
Lunde	455244.0944	8771614.043	1185	73.0	-56.514	
	455240.4369	8771676.73	1185	73.1	-52.238	
	455351.8146	8771683.514	1186	73.2	-52.897	
	455252.7095	8771595.908	1186	73.1	-52.422	
	455500.5204	8771604.85	1190	73.4	-49.665	
cluster 2	**455870.9065**	**8771063.335**			**-50.960**	**5.651**
Lomvi	455729.8663	8771045.728	1186	73.1	-51.455	
	455871.6151	8771056.554	1187	73.2	-49.661	
	455816.8746	8771131.397	1187	73.2	-51.292	
	455957.1214	8771047.601	1187	73.3	-51.035	
	455979.055	8771035.395	1187	73.2	-51.666	
cluster 3	**455615.6263**	**8770988.11**			**-56.517**	**1.572**
Lomvi	455615.6263	8770988.11	1183	72.9	-56.517	
					2012	
cluster 1	**455678.6715**	**8771256.849**			**-52.686**	**3.798**
Lomvi	455678.6715	8771256.849	1198	73.3	-52.686	
cluster 2	**455984.5214**	**8770899.162**			**-52.049**	**4.398**
Lomvi	456055.7961	8770911.362	1192	72.7	-52.735	
	455913.2466	8770886.962	1187	72.7	-51.456	
cluster 3	**455263.889**	**8771615.927**			**-52.292**	**4.159**
Lunde	455257.2689	8771638.371	1198	73.1	-52.276	
	455186.1878	8771661.976	1192	73.0	-51.547	
	455348.2103	8771547.435	1197	73.3	-53.210	
cluster 4	**455540.478**	**8771653.724**			**-52.456**	**4.004**
Lunde	455540.478	8771653.724	1200	73.4	-52.456	
cluster 5	**455784.4235**	**8771071.845**			**-53.112**	**3.443**
Lomvi	455822.1965	8771073.214	1198	73.2	-53.234	
	455746.6505	8771070.475	1194	73.1	-52.992	
					2013	
cluster 1	**455402.7595**	**8771555.159**			**-48.705**	**9.497**
Lunde	455516.7159	8771545.009	1191	73.8	-48.489	
	455562.7067	8771573.862	1191	73.8	-50.175	
	455366.2997	8771630.326	1191	73.7	-49.425	
	455430.5106	8771515.279	1192	73.8	-46.828	
	455513.297	8771504.632	1190	73.7	-46.895	
	455592.0678	8771599.788	1189	73.0	-51.341	
	455387.2268	8771566.18	1192	73.7	-49.971	
	455360.0374	8771543.686	1191	73.7	-47.539	
	455363.4735	8771445.498	1191	73.7	-48.646	
	455349.2105	8771583.004	1190	73.7	-49.196	
	455269.7169	8771518.124	1191	73.7	-49.534	
	455197.4109	8771584.243	1187	73.4	-47.939	
	455327.1997	8771607.437	1185	73.5	-49.650	

cluster 2	**456014.7212**	**8771098.663**			**-41.134**	**54.286**
Lomvi	455983.3382	8771075.959	1192	73.7	-46.326	
	456055.362	8771115.406	1191	73.7	-48.798	
	455962.6842	8771119.356	1193	73.7	-35.234	
	455988.7332	8771071.26	1189	73.7	-46.236	
	456083.4886	8771111.333	1186	73.0	-45.990	
cluster 3	**455913.3735**	**8771061.794**			**-46.656**	**15.222**
Lomvi	455893.8831	8771064.702	1189	73.6	-46.549	
	455863.2428	8771049.394	1187	73.6	-49.430	
	455982.9946	8771071.287	1188	73.6	-45.052	
cluster 4	**455653.2982**	**8771030.671**			**-46.694**	**15.093**
Lomvi	455678.0419	8771041.746	1188	73.5	-47.025	
	455628.5544	8771019.596	1185	73.5	-46.386	

ow rates ml/min		
r=3mm U=30cm/s	r=8mm U=15cm/s	r=8mm U=30cm/s
8.421	48.353	96.707
11.302	64.900	129.801
3.144	18.053	36.107
7.596	43.620	87.240
8.796	50.509	101.018
8.317	47.760	95.521
8.008	45.984	91.968
6.886	39.543	79.086
18.994	109.071	218.141

108.572	623.459	1246.918
30.445	174.823	349.645
30.186	173.336	346.671

	Lomvi		Lunde	
	min	max	min	max
a. Radius bubble size (mm)	3	8	3	8
b. Rising speed (cm s-1)	15	30	15	30
d. Calculated cluster flow rates (ml min-1)	3.4	101.0	4	95.5
e. Cluster flux ranges (mmol m-2 d-1)	13.3	395.5	15.7	374
f. Number of clusters	3		2	
g. Total flow rate (ml min-1)	11.6	267	8.2	187
h. Total output (ton y-1)	0.15	4.53	0.18	4.28